Comparing Properties of Common Bioinorganic Ligands with Switchable Variants of Cytochrome *c*

Fangfang Zhong, Stephanie L. Alden, Russell P. Hughes, and Ekaterina V. Pletneva*

Department of Chemistry, Dartmouth College, Hanover, NH 03755

*Corresponding author: ekaterina.pletneva@dartmouth.edu, Tel. 1-603-646-0933, Fax: 1-603-646-3946

ABSTRACT

Ligand substitution at the metal center is common in catalysis and signal transduction of metalloproteins. Understanding the effects of particular ligands, as well as the polypeptide surrounding, is critical for uncovering mechanisms of these biological processes and exploiting them in the design of bioinspired catalysts and molecular devices. A series of switchable K79G/M80X/F82C (X=Met, His, or Lys) variants of cytochrome (cyt) *c* was employed to directly compare stability of differently-ligated proteins and activation barriers for Met, His, and Lys replacement at the ferric heme iron. Studies of these variants and their non-switchable counterparts K79G/M80X have revealed stability trends Met < Lys < His and Lys < His < Met for the protein Fe^{III}-X and Fe^{II}-X species, respectively. The differences in the hydrogen-bonding interactions in folded proteins and in solvation of unbound X in the unfolded proteins explain these trends. Calculations of free energy of ligand dissociation in small heme model complexes reveal that the ease of Fe^{III}-X bond breaking increases in the series amine < imidazole < thioether, mirroring trends in hardness of these ligands. Experimental rate constants for X dissociation in differently-ligated cyt *c* variants are consistent with this sequence, but the differences between Met and His dissociation rates are attenuated because the former process is limited by heme crevice opening. Analyses of activation parameters and comparisons to those for the Lys-to-Met ligand switch in the alkaline transition suggest that ligand dissociation is entropically driven in all the variants and accompanied by Lys protonation at neutral pH. The described thiolate redox-linked switches have offered a wealth of new information about interactions of different protein-derived ligands with the heme iron in cyt *c* model proteins and we anticipate that the strategy of employing these switches could benefit studies of other redox metalloproteins and model complexes.

INTRODUCTION

The first coordination sphere of the metal ion and the immediate polypeptide surrounding are critical determinants of metalloprotein function. Substitution of a metal-bound ligand by another amino acid or small molecule is common in catalysis and signal transduction and plays a prominent role in metalloprotein folding reactions.[1-6] To understand mechanisms of ligand substitution in metalloproteins, both thermodynamic and kinetic factors need to be considered. While metalloprotein stability and its dependence on a particular ligand can be assessed with a multitude of experiments, including calorimetry,[7-9] electrochemistry,[10-12] and various protein denaturation methods,[9,13-14] options for investigation of ligand-substitution kinetics are more limited and primarily rely on either the addition of exogenous small ligands[15] or photolysis of the bound ligand.[16-17] These former methods require measurements at multiple concentrations of the exogenous ligand and may be complicated by difficulty achieving the high concentrations of the ligand that are often necessary to determine rates of ligand dissociation and by perturbations in protein structure such high ligand concentrations may cause.[18] The latter methods are more specialized and photolability of some ligands is low.[19] Voltammetry methods have been useful for some systems,[12] however, electrochemical studies of ligand-substitution kinetics may be complicated by protein interactions with the electrode.

In this report, we present the application of thiolate redox-linked switches to probe the role of the axial ligand at the heme iron on the polypeptide-tuned barriers to ligand substitution. Redox-dependent ligand switch involving Cys is not only important for activation and regulation of signaling function of heme sensors but could also contribute to deactivation of thiolate-ligated metalloenzymes.[20-21] Since the intrinsic affinity of thiolate for ferric heme iron is greater than those of other common amino-acid ligands X (Met, His, and Lys) and that of thiol for ferrous heme iron,[5,14,22] X-to-Cys and Cys-to-X ligand switches can be triggered by oxidation and reduction of the heme iron, respectively. Redox-linked Cys-to-His and Cys-to-Met switches at the heme iron have been described for a number of native proteins.[2,21,23-25] In our work with model proteins we have shown that redox-linked Cys-to-Met switch can also be engineered within a protein scaffold and described kinetics of Met-to-Cys ligand substitution upon oxidation of the heme iron in the T78C/K79G variant of cytochrome (cyt) *c*.[26] For this variant, the Met-ligated ferric intermediate

can be readily observed, and the rate-limiting step in the Met-to-Cys ligand-switching reaction is deprotonation of the incoming Cys78.

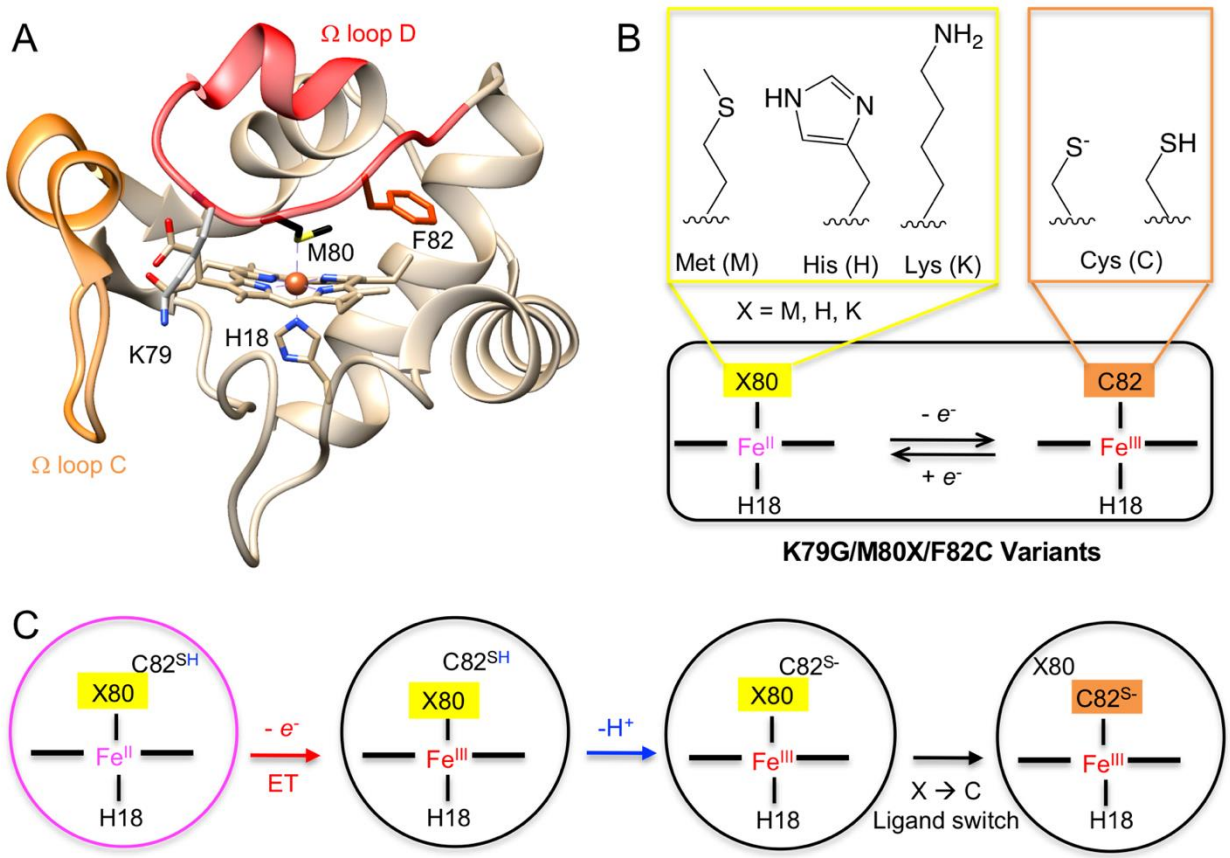

Figure 1. (A) Structure of yeast *iso*-1 cyt *c* (PDB ID: 2YCC[27]) showing positions of axial ligands His18 and Met80 and two mutation sites (Lys79 and Phe82) in the variants in this study. (B) Structures of Met, His, Lys, and Cys sidechains. The engineered variants K79G/M80X/F82C undergo a switch from X80 to Cys82 ligation upon oxidation of the heme iron. (C) A scheme depicting steps in the overall reaction.

We have wondered if substitution of other ligands to the ferric heme iron can be examined through this approach, allowing direct comparison of associated barriers for Met, His, and Lys replacement within the same polypeptide scaffold. In order to focus on the ligand-substitution processes rather than deprotonation of the incoming Cys, we have designed a series of cyt *c* variants K79G/M80X/F82C (X= Met, His, and Lys; Figure 1) with Cys installed at position 82, to minimize the likelihood interactions of this Cys with other residues and increase the flexibility of

the heme coordination Ω-loop D. The bulky hydrophobic Phe82 is highly conserved in cyt *c* proteins and contributes to the stabilization of the heme crevice.[28-29] Mutations at this site have been shown to increase dynamics of the heme crevice and decrease protein stability.[30-31] Since in destabilized variants of cyt *c* Lys79 may coordinate to the ferric heme iron already at near neutral pH,[31] this residue was replaced to Gly to avoid Lys79 competing with X for coordination to the heme iron.

Herein, we show that K79G/M80X/F82C cyt *c* proteins undergo X-to-Cys82 ligand switch upon oxidation of the heme iron, allowing for convenient determination of ligand substitution rates of the ferric heme iron and corresponding activation parameters. With this approach, complemented by density-functional-theory (DFT) calculations, molecular dynamics (MD) simulations, and studies of non-switchable K79G/M80X variants, we compare ligand-substitution kinetics of the three ligands and the influence of the surrounding protein on the dissociation process. Thermodynamic analyses reveal the influence of a particular ligand on protein stability and reduction potentials. Investigations of switchable variants also offer insights into the mechanism of the alkaline transition in cyt *c*, the functionally-relevant switch from Met-to-Lys ligation at the heme iron at high pH.[1,32-37] Systematic studies of differently-ligated heme proteins and models in this work enhance our current understanding of heme sensors, enzymes, and electron-transfer (ET) carriers, and may prove useful in the design of bioinspired catalysts and molecular devices.

MATERIALS AND METHODS

General. All chemicals were purchased from Fisher Scientific Inc. and VWR International, unless noted otherwise. Buffers were prepared using reagent-grade chemicals. Water was purified to a resistivity of 18.2 MΩ cm using Barnstead E-Pure Ultrapure Water Purification System. All experiments were performed at room temperature unless stated otherwise.

Data analyses were carried out using MATLAB_R2019a (MathWorks) and Python 3.[38] Images were produced using UCSF Chimera.[39]

Site-Directed Mutagenesis, Protein Expression and Purification. All the variants in this work were created using the Rbs (WT*) plasmid[40] as a template, and point mutations were introduced with a Quikchange kit (Agilent Technologies, Inc.). The parent WT* cyt *c* had two background mutations, K72A and C102S, to prevent Lys72 misligation to the heme and formation of protein dimers through Cys102, respectively. In addition to these two background mutations, K79G/M80K* also had K73A mutation; we have partially characterized this protein in our prior work and referred to it in those studies as M80K$^{\#}$.[41] For consistency with other variants and the ease of abbreviation in the current work, we refer to M80K$^{\#}$ here as K79G/M80K*. Plasmids were extracted using a QIAprep Spin Miniprep Kit (Qiagen), and the desired mutations were confirmed by gene sequencing at the Molecular Biology & Proteomics Core Facility (Dartmouth College). Expression and purification of the proteins were carried out following the published procedures.[42] Protein extinction coefficients were determined by the pyridine hemochrome assay.[43]

Spectroscopic Measurements. Oxidation and reduction of the heme iron in protein variants were achieved by adding potassium ferricyanide and sodium dithionite, respectively. Excess redox reagents were removed with a PD10 desalting column (GE Healthcare). Ferrous proteins were prepared under anaerobic conditions in a nitrogen-filled glove box (COY Laboratory Products). Electronic absorption spectra were collected on an Agilent 8453 diode-array spectrophotometer. Circular dichroism (CD) spectra were recorded on a J815 CD spectropolarimeter equipped with a variable temperature Peltier cell device (JASCO). Thermal denaturation, pH titrations, and spectroelectrochemistry measurements were performed and analyzed as previously described.[14,44] Stopped-flow mixing experiments were done using a BioLogic SFM-300 instrument and absorption spectra were recorded with a diode-array detector (Model TIDAS S 300 K from J&M ANALYTIK AG); the mixing deadtime under our experimental conditions was 7.5 ms.

EPR spectra were recorded on a Bruker EMX 300 X-band EPR spectrometer (Bruker Biosciences Corp.) at 10 K. Experimental parameters (9.49 GHz microwave frequency, 3.21 mW microwave power, 100 kHz modulation frequency, 1.00 G modulation amplitude and a 20.48 ms time constant) were adapted from previous studies of cyt *c* proteins.[41] Before measurements, proteins were treated with excess of potassium ferricyanide to achieve full conversion to ferric forms, repurified, and concentrated to about 500 μM. All samples were prepared in a 100 mM sodium phosphate buffer at pH 7.4.

^{1}H NMR spectra were recorded on a 500 MHz Bruker NMR spectrometer (Bruker Biosciences). Freshly prepared samples of ferric proteins were exchanged into 100% D_2O buffered with 50 mM sodium phosphate at pD 7.4. Ferrous samples were prepared in a 50 mM sodium phosphate buffer at pH 7.4 or in a 50 mM sodium borate at pH 10, both containing 10% (v/v) D_2O; 5 mM sodium dithionite was kept in the solution to ensure the heme iron stayed reduced during measurements. Data collection and analyses were done as previously described.[41]

Studies of Azide (Az) Binding. All experiments were carried out with ferric variants in a 100 mM sodium phosphate buffer at pH 7.4. Equilibrium binding measurements were performed by mixing the protein at 10-16 μM and solutions of sodium azide (Az) at a series of concentrations with a volume ratio of 1:1. The final concentration of proteins in these measurements was between 5 and 8 μM and the concentrations of Az were increased from 0 to 500 mM or until no more spectral changes occurred. Samples were equilibrated for at least 30 min upon the addition of Az, and then absorption spectra were recorded. The difference spectra (with and without Az) were used to determine wavelengths with maximum change in absorbance upon the Az binding. Changes in the Soret absorption band with increasing Az concentrations were fit to eq 1[45] to determine apparent binding constants (K_a^{Az}), where [cyt] is the total concentration of cyt *c*.

$$\Delta A=\frac{\Delta A_{max}}{2[cyt]\times K_a^{Az}}\left\{1+[cyt]\times K_a^{Az}+[Az]\times K_a^{Az}-\left((1+[cyt]\times K_a^{Az}+[Az]\times K_a^{Az})^2-4[cyt]\times[Az]\times(K_a^{Az})^2\right)^{0.5}\right\} \quad \text{(eq 1)}$$

Binding of Az to cyt *c* has been previously described as a two-step process consisting of the dissociation of the endogenous ligand (Met80 in the wild-type cyt *c*) concomitant with conformational changes in the protein, followed by binding of Az to the heme iron (Scheme 1).[15] Parameters k_{off}^X and k_{on}^X are rate constants for the dissociation and rebinding of ligand X, respectively. Parameters k_{on}^{Az} and k_{off}^{Az} are rate constants for the binding and dissociation of Az,

respectively. The binding constant K_a^{Az} is a composite of the four rate constants k_{off}^{X}, k_{on}^{Az}, k_{on}^{X}, and k_{off}^{Az} (eq 2), and the coefficient α reflects the fraction of the Az-bound form (eq 3). The observed rate constant k_{obs}^{Az} is described by eq 4.

$$\text{X-Fe}^{3+}\text{-His} \underset{k_{on}^{X}}{\overset{k_{off}^{X}}{\rightleftharpoons}} \text{Fe}^{3+}\text{-His}$$

$$\text{Fe}^{3+}\text{-His} + \text{Az} \underset{k_{off}^{Az}}{\overset{k_{on}^{Az}}{\rightleftharpoons}} \text{Az-Fe}^{3+}\text{-His}$$

Scheme 1. Replacement of endogenous ligand X by Az in 6c heme iron proteins.

$$K_a^{Az} = \frac{k_{off}^{X} \times k_{on}^{Az}}{k_{on}^{X} \times k_{off}^{Az}} \quad \text{(eq 2)}$$

$$\alpha = \frac{K_a^{Az} \times [Az]}{1 + K_a^{Az} \times [Az]} \quad \text{(eq 3)}$$

$$\alpha k_{obs}^{Az} = \frac{k_{off}^{X} \times k_{off}^{Az} \times K_a^{Az} \times [Az]}{k_{off}^{Az} \times K_a^{Az} \times [Az] + k_{off}^{X}} \quad \text{(eq 4)}$$

Kinetics of Az binding were monitored by following time courses of changes in the Soret absorption band upon mixing of solutions of protein and Az. For K79G/M80K*, mixing was done manually by pipetting, and absorbance spectra were recorded with an Agilent 8453 diode-array spectrophotometer. For K79G, M80A, and K79G/M80H, mixing was done using the stopped-flow instrument. The time courses of $Abs_{415\ nm}$ were fit to a monoexponential equation to yield the observed rate constants k_{obs}^{Az}. The dependence of k_{obs}^{Az} values on Az concentration was then fit to eq 4 to yield k_{off}^{X} for the ligand X dissociation process.[15] For K79G/M80K*, rate constants were similar at all concentrations of Az employed, and the averaged value of k_{obs}^{Az} from these measurements was taken as k_{off}^{X}. The activation energy $\Delta G^{\ddagger}(X)$ at room temperature for the ligand X dissociation was calculated from rate constants k_{off}^{X} using eq 5 ($k = k_{off}^{X}$)[46] where R, k_B, and h are gas, Boltzmann's, and Planck's constants, respectively, and T is temperature in Kelvin.

$$\Delta G^{\ddagger} = RT \times (\ln(\frac{k_B}{h}) - \ln(\frac{k}{T})) = RT \times (\ln(\frac{k_B T}{h}) - \ln k) \quad \text{(eq 5)}$$

Kinetics of Oxidation of Ferrous K79G/M80X/F82C Variants. Kinetic studies of oxidation of ferrous K79G/M80X/F82C variants by $Fe(CN)_6^{3-}$ and $Co(phen)_3^{3+}$ were performed as previously described.[26] Solutions of proteins and small-molecule oxidants were prepared in a degassed 10 mM sodium phosphate buffer at pH 7.4 containing 100 mM NaCl. The concentrations of $Fe(CN)_6^{3-}$ and $Co(phen)_3^{3+}$ were determined with electronic absorption spectra using $\varepsilon_{420} = 1.04$ $mM^{-1}cm^{-1}$ and $\varepsilon_{303} = 19.2$ $mM^{-1}cm^{-1}$, respectively.[47-48] The stopped-flow instrument was used to initiate the reactions, except for studies of K79G/M80K*/F82C, for which mixing was done manually. Temperature in the stopped-flow and manual mixing experiments was controlled with a NESLAB RTE-111 water bath and an Agilent 89090A Peltier temperature controller, respectively. The temperature readings for stopped-flow reactions were directly recorded from a temperature probe (Model 058-10 from BioLogic, USA) installed close to the reaction cuvette. All the measurements were done under nitrogen atmosphere to maintain anaerobic conditions. For reactions with $Fe(CN)_6^{3-}$, absorption changes in the spectral range from 500 to 800 nm were monitored; final concentrations were about 50 μM for proteins and from 0.3 to 1.5 mM for $Fe(CN)_6^{3-}$. For reactions with $Co(phen)_3^{3+}$, absorption changes in the spectral range from 350 to 650 nm were monitored; the final concentrations were about 8 μM for proteins and from 0.1 to 1 mM for $Co(phen)_3^{3+}$. The temperature dependencies of rate constants were fit to eq 6 ($k = k^{X\text{-}C}$) to yield activation parameters $\Delta H^{\ddagger}$(X-C) and $\Delta S^{\ddagger}$(X-C) for X-C ligand switches. Activation free energies $\Delta G^{\ddagger}$(X-C) were calculated as $\Delta H^{\ddagger}$(X-C)-$T\Delta S^{\ddagger}$(X-C).

$$\ln(\frac{k}{T}) = -\frac{\Delta H^{\ddagger}}{RT} + \ln(\frac{k_B}{h}) + \frac{\Delta S^{\ddagger}}{R} \qquad \text{(eq 6)}$$

Kinetics of Downward pH Jump. Lyophilized horse heart (*hh*) cyt *c* protein (Sigma-Aldrich) was dissolved in an aqueous solution containing 100 mM NaCl at a protein concentration about 50 μM, and the initial pH was adjusted to 10.0 by adding NaOH. The final pH was achieved by mixing the protein solution with a 12 mM sodium phosphate buffer at pH 7.0 or 7.5 containing 100 mM NaCl in a volume ratio of 1:5 by the stopped-flow instrument. Absorption changes in the spectral range from 350 to 650 nm were monitored, and the observed rate constants k_{obs}^{pH} were derived from fits of the time courses of the absorbance in the full range of monitored wavelengths to a monoexponential equation using SFit software (BioLogic). The previously described mechanism for the alkaline transition was considered (Scheme 2),[49] where K_H is the ionization

constant for a group triggering the alkaline transition. k_f and k_b are rate constants for forward Met-to-Lys and back Lys-to-Met reactions, respectively. The dependence of k_{obs}^{pH} on $[H^+]$ is defined by eq 7. When $[H^+] \gg K_H$, k_{obs}^{pH} is approximately equal to k_b. Thus, k_b was determined by averaging the k_{obs}^{pH} values under our experimental conditions. Activation parameters $\Delta H^{\ddagger}$ and $\Delta S^{\ddagger}$ for the back reaction were obtained by fitting the temperature dependence of k_b to eq 6.

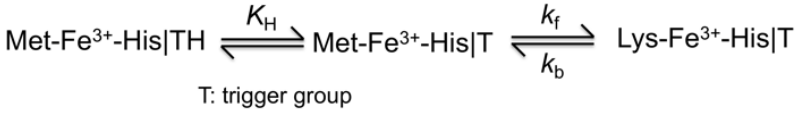

Scheme 2. Mechanism of the alkaline transition of cyt *c*.

$$k_{obs}^{pH} = k_b + k_f \frac{K_H}{K_H + [H^+]} \quad \text{(eq 7)}$$

MD Simulations. Structural models of ferric and ferrous variants were constructed based on the crystal structures of ferric (PDB ID: 2YCC)[27] and ferrous (PDB ID: 1YCC)[50] yeast *iso*-1 cyt *c*. Not Just a Molecular Dynamics (NAMD) was used for simulations, and structural analysis was performed by Visual Molecular Dynamics (VMD). For the variants with Cys-, Met- or His-ligated heme iron, previously described patches were used to link the ligand to the iron.[51-52] The topology and parameters information for Lys coordination to heme iron was adopted from a recent work in our group.[53] The solvation of protein structure was achieved by adding a water box of TIP3 model, which extended 12 Å from the protein surface. Then the Autoionize plug-in of VMD was used to add Na^+ and Cl^- ions with an ionic strength of 0.15 M. In the case of the Lys-ligates species, explicit exclusions of the interactions between the positively charged hydrogen atoms (HZ1 and HZ2 atoms) of the amine group of Lys80 ligand and the negatively charged nitrogen atoms of the porphyrin (NA, NB, NC, ND atoms) and His18 ligand (NE2 atom), resulting in ten exclusion pairs (HZ1-NA, HZ1-NB, HZ1-NC, HZ1-ND, HZ1-NE2, HZ2-NA, HZ2-NB, HZ2-NC, HZ2-ND, HZ2-NE2) were introduced into the protein structure file. The resulting system was first minimized for 5,000 steps with conjugate gradients using CHARMM22 force field parameters[54] for geometry optimization and further equilibrated for 25,000,000 steps (2 fs per step, 50 ns in total) at 300 K and 1 atm using the Langevin piston method. Periodic boundary conditions were employed. The trajectory data were saved every 10,000 steps (20 ps). The trajectory files were loaded and the residue-to-residue distances defined by the closest distance between any two non-hydrogen atoms

in the residue pair were calculated with MDAnalysis toolkit[55] in Python 3. The contact frequencies with a distance cutoff of 10 Å were calculated, and heat maps of contact frequencies were generated in Python 3. Hydrogen bonds (Donor-Acceptor distance cutoff of 3.5 Å and angle cutoff of 20 degrees) in all the MD frames were extracted, and the appearance frequencies were calculated in VMD using the Hydrogen Bonds Plugin. Solvent-accessible surface areas (SASA) for the heme were calculated in VMD using a probe radius of 1.4 Å.

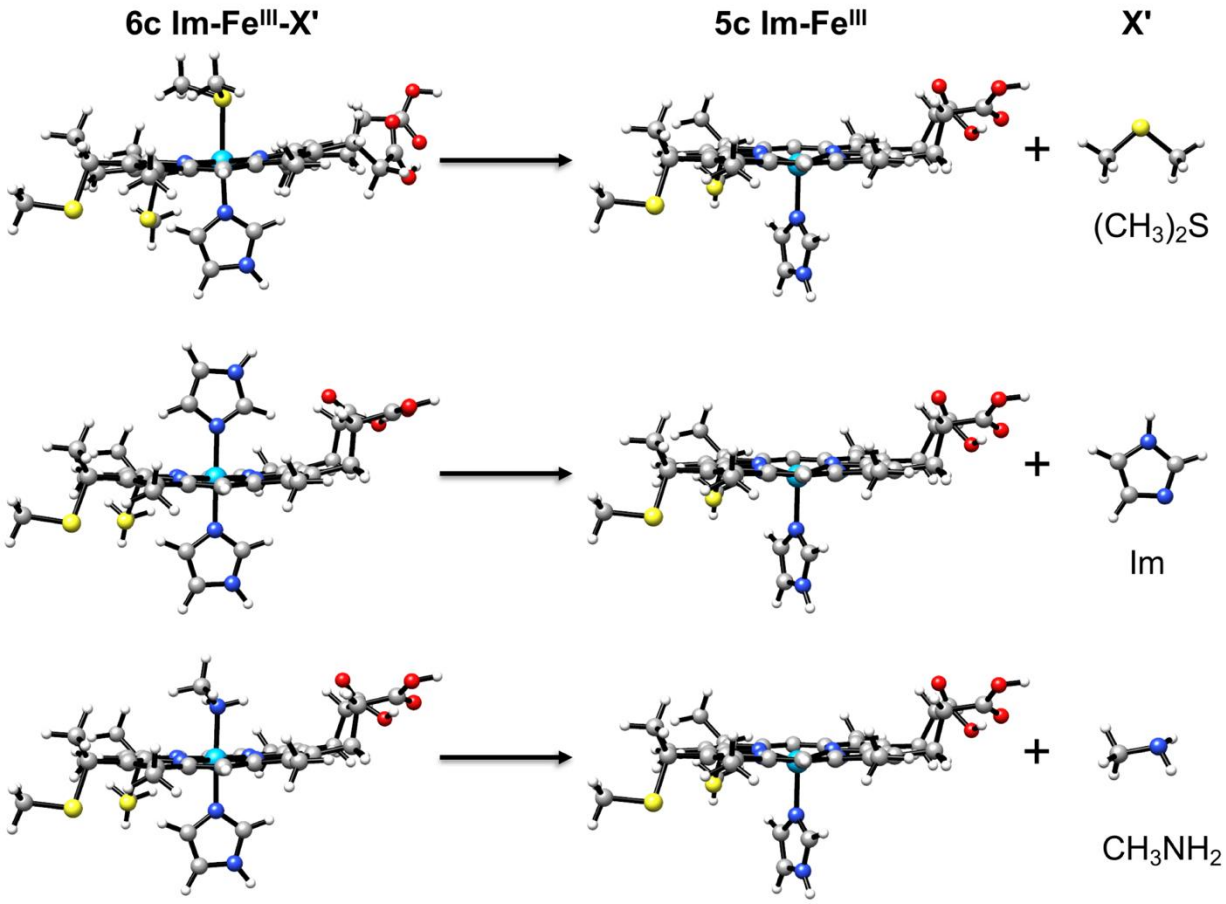

Figure 2. Conversions of the **6c** heme complexes into the **5c** heme species and the dissociated ligand X'. Small molecules X' ($(CH_3)_2S$, Im, and CH_3NH_2) mimic side chains of Met, His, and Lys, respectively.

DFT Calculations. Small ligands X′ dimethylsulfide ($(CH_3)_2S$), imidazole (Im), and methyl amine (CH_3NH_2) were used as mimics of side chains of Met, His and Lys, respectively (Figure 2).

Six-coordinate (**6c**, Im-Fe^{III}-X′ and Im-Fe^{III}-H_2O) and five-coordinate (**5c**, Im-Fe^{III}) heme models were constructed with two thioether bonds added to the two vinyl positions of the heme to mimic thioether linkages of the *c*-type heme. Full-molecule geometry optimizations and calculations of vibrational frequencies were carried out using the B3LYP[56-60] functional with the zero-damping, two-body only D3 correction of Grimme *et al*.,[61-62] and the LACV3P** basis set, which uses Los Alamos Core potentials for the transition metal,[63-66] and the 6-311G** basis for all lighter atoms,[67-70] as implemented in the Jaguar[71-72] suite of programs from Schrodinger. Spin states used for each calculation were low-spin (doublet) for Im-Fe^{III}-X′ and high-spin (sextet) for Im-Fe^{III}-H_2O and **5c** Im-Fe^{III}.[73-74] Computed structures were confirmed as those corresponding to energy minima by calculating vibrational frequencies with second-derivative analyses methods and confirming the absence of imaginary frequencies. Solvation corrections were made using single-point energy computations with the Poisson-Boltzmann implicit H_2O solvent model[75-76] as implemented in Jaguar. Default options were chosen in Jaguar except for the following: molecular symmetry was not used; energy convergence and root-mean-square density matrix convergence criteria were set at 1.00E-05 and 1.00E-06 Hartrees, respectively; and the highest accuracy cutoffs were used in the Self-Consistent Field (SCF) calculations. Electronic plus nuclear energy (E), zero-point-energy (E_{ZPE}), solvation free energy (G_{solv}), internal energy (U) and the entropy (S) were computed for each component using B3LYP-D3/LACV3P**(H_2O) and B3LYP-D3/LACV3P**(gas). The change in Gibbs free energy was calculated as $\Delta G = \Delta E + \Delta G_{solv} + \Delta E_{ZPE} + \Delta U + nRT - T\Delta S_{(gas)}$ at 298 K and 1 atm.

RESULTS

Relative Energies of Differently-Ligated Heme Model Complexes and Ligand Dissociation Energies from DFT Calculations. Coordinates of energy-minimized structures of **5c** and **6c** heme model complexes in Figure 2 are provided in the Supporting Information. The free energies of the **6c** Im-Fe^{III}-X′ heme complexes follow the trend CH_3NH_2 > Im > $(CH_3)_2S$ in the gas phase (Table S1). The values of the solvation energy in H_2O are similar for the three Im-Fe^{III}-X′ model complexes (Table S1), preserving the trend observed in the gas phase, but solvation energies of the ligands X′ are distinct. When accounted for all the species, the Δ*G* values for the formation of the **6c** Im-Fe^{III}-X′ complexes from **6c** Im-Fe^{III}-H_2O and X′ suggest the following trend for these amino-acid mimics: $(CH_3)_2S$ > Im > CH_3NH_2 (Figure S1), which is qualitatively consistent with that from experimental studies of ligand binding to heme-containing peptides microperoxidases (MPs).[5,41] Upon also taking into account protonation of unbound CH_3NH_2 in aqueous solution at pH 7,[77] the difference between Δ*G* values for the formation the Im-Fe^{III}-Im and Im-Fe^{III}-CH_3NH_2 from Im-Fe^{III}-H_2O becomes smaller, but the overall trend $(CH_3)_2S$ > Im > CH_3NH_2 for the three ligands X′ does not change (Figure S1). However, upon taking into account protonation of the unbound Lys ligand in MP binding equilibria, the trend in Δ*G* values is modified (Met ≈ Lys > Im, Figure S1), suggesting that additional factors, not captured by computational analyses of small porphyrin and amino-acid X′ mimics, might be in play here.

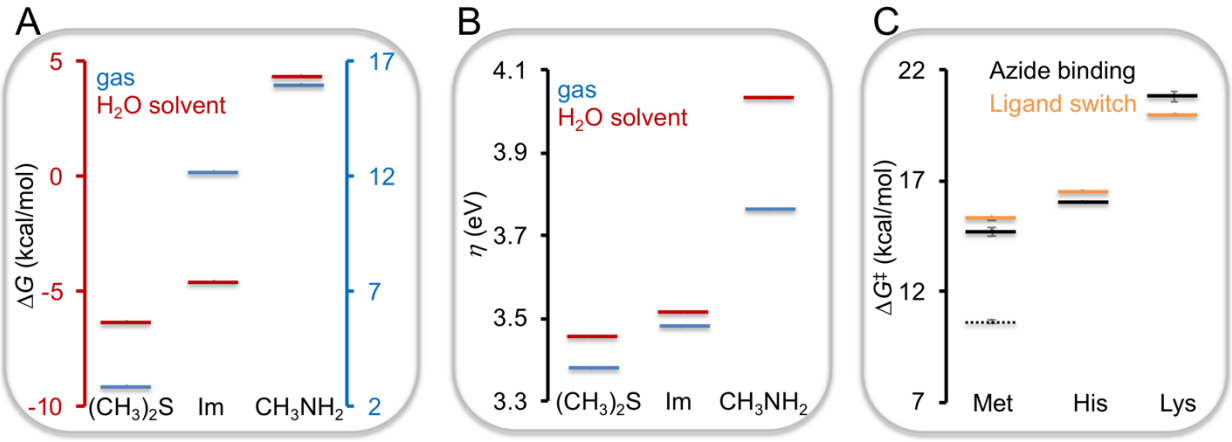

Figure 3. (A) Free energy diagrams for the conversion of **6c** heme complexes into **5c** heme species and X′ in Figure 2 using DFT-derived energy values in Table S1. For the solvated species, free

energies were calculated as G=G_{gas}+G_{solv}+G_{ZPE}. (B) Hardness of ligands X′ calculated from DFT-derived orbital energies using $\eta = (\varepsilon_{LUMO}-\varepsilon_{HOMO})/2$.[78] (C) Activation free energies $\Delta G^{\ddagger}$ derived from experimental kinetics of Az replacements (*black*) and redox-linked X-to-Cys ligand-switching processes (*orange*). The parameter $\Delta G^{\ddagger}$ was calculated using eq 5 with k_{off}^{X} and $k^{X\text{-}C}$ values at 298 K. The *dash* line represents the free energy of activation for Fe^{III}-S(Met) bond breaking (9×10^4 s^{-1}) estimated from rate constants k_{obs}^{NO} for NO rebinding upon laser photolysis of the NO-bound ferric cyt *c*.[79]

The ΔG values for the dissociation of the ligand X′ from the **6c** Im-Fe^{III}-X′ heme adducts to form **5c** Im-Fe^{III} and X′ reflect the activation free energy $\Delta G^{\ddagger}$ for dissociation of ligand X′ from the heme iron. The trends in these values (Figure 3) observed with these small model complexes, both in the gas phase and in H_2O, suggest the following sequence for the rates of dissociation of X′: $(CH_3)_2S$ > Im > CH_3NH_2.

The out-of-plane distortions of the heme group are common in heme proteins.[80-81] Ruffling, which involves twisting of the four pyrrole rings along the Fe-$N_{pyrrole}$ bonds, is particularly prominent in *c*-type hemes.[80] Previous studies of heme *c* peptides suggested that the CXXCH heme attachment itself can induce heme ruffling.[82-83] Since model structures in this study include two covalent thioether linkages to the porphyrin and an Im ligand coordinated to the iron to mimic the CXXCH heme attachment, comparison of these structures allows for the evaluation of a particular ligand X′ on the deformation of *c*-type heme. The out-of-plane distortions of the porphyrin in the heme models are tabulated in Table S2. Ruffling of the heme decreases in the series $(CH_3)_2S$ > Im > CH_3NH_2. An decrease in ruffling has been linked to the increase in the tetragonal field Δ/λ term by preferentially raising the energy of the d_{xy} orbital of the iron center.[84]

Non-switchable Variants of Cyt *c*. Variants K79G, K79G/M80H, and K79G/M80K* were prepared to serve as model proteins that do not undergo switching processes of endogenous ligands at pH 7.4 and have the same X-ligation to the heme iron (X= Met, His, and Lys, respectively) in both ferric and ferrous forms. We have previously shown that the heme iron is ligated by Met80 in both ferric and ferrous K79G at pH 7.4.[41] Similarly, Lys80 is the ligand to the heme iron in both ferric and ferrous K79G/M80K* at pH 7.4. [41,44]

Table 1. Positions (in nm) and Extinction Coefficients (in $mM^{-1}cm^{-1}$) of Characteristic Bands in Electronic Absorption Spectra of Yeast *iso*-1 Cyt *c* Variants Studied or Referred to in This Work[a,b]

Variant	*Ferric*				*Ferrous*		
	δ	Soret (γ)	β, α	near-IR	Soret (γ)	β	α
K79G[c]	363 (28.8)	409 (110.0)	528 (10.8)	695 (0.8)	415 (135.7)	520 (17.3)	549 (29.4)
M80H	353 (29.1)	407 (135.1)	535 (11.1)	--	417 (147.0)	521 (12.6)	550 (20.9)
K79G/M80H	353 (28.1)	406 (124.3)	530 (10.7)	--	417 (197.5)	522 (16.3)	550 (30.8)
K79G/M80K*[c]	357 (25.3)	404 (117.2)	528 (9.4)	--	416 (184.5)	520 (13.2)	550 (27.8)
K79G/F82C	357 (32.3)	416 (89.5)	538 (8.8)	~635, 710 (1.3)	415 (125.1)	520 (15.4)	549 (26.3)
K79G/M80H/F82C	354 (34.3)	415 (95.1)	539 (9.4)	~635, 708 (1.2)	415 (176.6)	520 (15.6)	549 (32.0)
K79G/M80K*/F82C	354 (33.6)	416 (94.4)	537 (9.1)	~635, 707 (1.3)	416 (175.6)	520 (15.1)	550 (29.4)

[a]Extinction coefficients are given in parentheses. [b]At pH 7.4 and room temperature. [c]From studies of Amacher *et al*.[41]

The position and intensity of the Soret band at 406 nm in ferric K79G/M80H at pH 7.4 are consistent with a **6c** low-spin heme iron species (Table 1, Figure S2). EPR and ^{1}H NMR spectra (Table S3, Figure S2) display signals resembling those of known **6c** His-ligated ferric heme proteins,[85-86] suggesting the same ligation in ferric K79G/M80H. The electronic absorption spectrum of ferrous K79G/M80H is indicative of a **6c** low-spin heme iron as well (Table 1). Two small and broad signals are observed in the ^{1}H NMR spectrum of ferrous M80H at pH 7.4, but they are not detectable in the spectrum of ferrous K79G/M80H (Figure S3), possibly because an additional K79G mutation makes the heme environment more dynamic; such behavior is not uncommon in heme proteins.[87] We have tested whether a Lys residue could ligate to the heme iron instead of His80. Ferrous cyt *c* with the Lys-ligated heme iron shows a characteristic feature of four signals with identical intensity observed in the upfield region corresponding to four protons from the methylenes of the Lys residue. This feature is readily apparent in the spectrum of K79G/M80H at pH 10 (Figure S3) but is absent at pH 7.4. These findings, together with the reduction potential of K79G/M80H being similar to that of M80H and typical of His-ligated heme iron species (Table S4), suggest that His80 is also the ligand to the heme iron in K79G/M80H. Global stability of M80H is similar to that of WT* in the ferric state but is less in the ferrous state (Table S5 and S6). The introduction of the K79G substitution to WT* and M80H proteins yield similar destabilizing effects, corroborating our previous findings of the effects of this mutation on cyt *c* structure.[88]

The Δ/λ parameters calculated from EPR data are 2.96, 3.11 and 2.80 for K79G, K79G/M80H and K79G/M80K*, respectively. The trend in these experimental parameters is in accord with the differences in ruffling predicted for the thioether- and Im-ligated models in our DFT analyses. The amine-ligated model, however, does not follow the experimental trend of protein variants, suggesting that the surrounding polypeptide in the Lys-ligated K79G/M80K* may play a role in deforming the heme and altering its electronic structure.

To explore structural variations among the differently-ligated cyt *c* variants, MD simulations of K79G, K79G/M80H, and K79G/M80K* were performed. The heat maps of contact frequencies for the regions corresponding to the Ω-loop C, 60´s helix, Ω-loop D, and the heme group are plotted in Figure S4. To enable a more straightforward pairwise comparison of particular species, corresponding heat maps are overlayed in Figure S5. The simulated structures of ferric K79G,

K79G/M80H, and K79G/M80K* display very similar intramolecular contacts. The contacts in ferrous Met-ligated K79G and Lys-ligated K79G/M80K* are also similar. The higher frequencies of multiple contacts in these ferrous proteins compared to those in their ferric counterparts suggest a decrease in the polypeptide dynamics upon the heme iron reduction. In contrast, the lower contact frequencies in ferrous His-ligated K79G/M80H suggest that this protein is more dynamic than ferric K79G/M80H or ferrous K79G and K79G/M80K*.

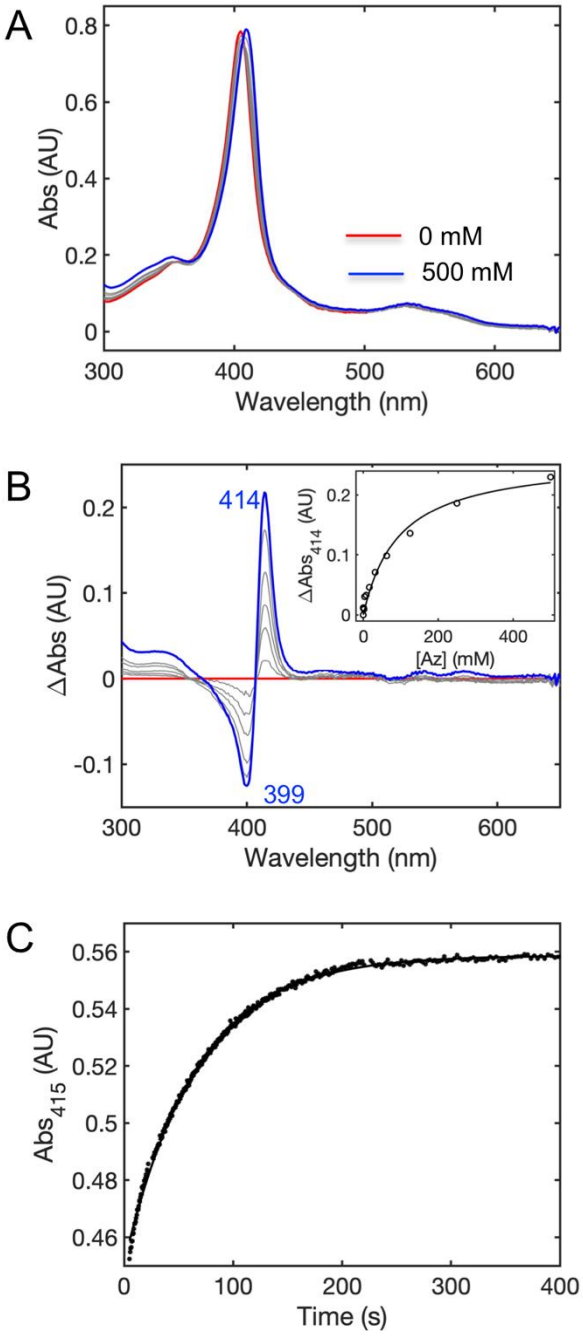

Figure 4. (A) Electronic absorption spectra of ferric K79G/M80K* with and without 500 mM Az. (B) The difference spectra from the data in panel A. (*Inset*) The absorbance changes at 414 nm ΔAbs_{414} at different Az concentrations. Fits of these data to eq 1 yielded K_a^{Az} in Table 2. (C) A representative time course of absorbance at 415 nm for K79G/M80K* upon binding of 500 mM Az. The time course was fit to a monoexponential equation to yield the observed rate constant k_{obs}^{Az} for further analyses in Figure S6.

Ligand Dissociation in Non-Switchable Variants Examined by Az Replacement. Several small ligands, including Az, bind the heme iron of cyt *c*.[15] The equilibrium titrations of ferric cyt *c* variants with Az yielded apparent binding constants K_a^{Az} for the series (Figures 4A and 4B, Table 2); these values depend on the flexibility of the heme crevice and the ease of dissociation of the endogenous heme ligand.[15,30]

Parameters from Az binding kinetic studies (Figure 4C) are summarized in Table 2. For K79G and K79G/M80H, the saturation effect is evident for the dependence of k_{obs}^{Az} on Az concentration and rate constants k_{off}^{X}, k_{off}^{Az}, and k_{on}^{Az}/k_{on}^{X} can be readily obtained (Figures S6A and S6B). For K79G/M80K*, the observed rate constant k_{obs}^{Az} does not change with Az concentration (Figure S6C), suggesting that k_{obs}^{Az} reaches the limiting-rate value k_{off}^{X} even at the lowest concentration of Az in our experiments.

Trends in calculated $\Delta G^{\ddagger}(X)$ values from the rate-limiting process described by k_{off}^{X} from the Az binding experiments mirror the relative order of $\Delta G^{\ddagger}(X)$ values predicted from our DFT calculations (Figure 3C and Table 3), but the energy values themselves are distinct. We explore whether a true ligand dissociation process or other processes limit Az binding kinetics in these proteins with our studies of substitution of these ligands X in switchable variants and subsequent analyses.

Table 2. Affinities and Rate Constants from Azide (Az) Binding Experiments for Cyt *c* Variants Studied or Referred to in This Work[a]

Variant[b]	X	K_a^{Az} (M^{-1})	K_d^{Az} (mM)	k_{off}^{X} (s^{-1})	k_{off}^{Az} (s^{-1})	$\frac{k_{on}^{Az}}{k_{on}^{X}}$ (M^{-1})
WT[c]	Met	16.7 ±0.6	60 ± 2	74 ± 20	1.7 ± 0.1	0.4 ± 0.1
K79G	Met	48.1 ± 3.7	20.8 ± 1.6	92 ± 26	8.6 ± 2.7	4.5 ± 1.9
M80A	OH^-	$(1.2 \pm 0.3)\times10^5$	0.0086 ± 0.0023	7.9 ± 0.6	N/A[d]	N/A[d]
K79G/M80H	His (+minor OH^-)	34.6 ± 7.4	28.9 ± 6.2	4.4 ± 0.2	6.0 ± 0.7	47.4 ± 11.7
K79G/M80K*	Lys	10.1 ± 1.5	98.9 ± 15.1	0.013 ± 0.001	N/A[d]	N/A[d]
hh WT[e]	Met	4.5	222	31 ± 10	5.2 ± 0.3	0.82
hh M80H	His	99.0 ± 16.7	10.1 ± 1.7	5.1 ± 0.2	N/A[d]	N/A[d]

[a]At pH 7.4 and room temperature, unless specified otherwise. [b]All entries, except for the last two, are for variants of yeast *iso*-1 cyt *c*. [c]The variant expressed in yeast, having C102T mutation and trimethyl-Lys72 from studies of Rafferty *et al.*[30] at pH 6.0. [d]Not available. [e]From studies of Sutin and Yandell[15] at pH 7.0.

Table 3. Activation Free Energies for the X-to-Cys Ligand-Switching Processes in K79G/M80X/F82C Cyt *c* Variants and Ligand Dissociation in the Corresponding Non-Switchable K79G/M80X Variants[a]

	X-to-Cys Ligand Switch			Ligand X Dissociation		
X	Variant	$k^{X\text{-}C}$ (s^{-1})[b]	$\Delta G^{\ddagger}$(X-C) (kcal/mol)	Variant	k_{off}^{X} (s^{-1})[c]	$\Delta G^{\ddagger}$(X) (kcal/mol)
Met	K79G/F82C	34 ± 2	15.3 ± 0.1	K79G	92 ± 26	14.7 ± 0.2
His	K79G/M80H/F82C	4.4 ± 0.2	16.5 ± 0.1	K79G/M80H	4.4 ± 0.2	16.5 ± 0.1
Lys	K79G/M80K/F82C	0.012 ± 0.001	20.0 ± 0.1	K79G/M80K*	0.013 ± 0.001	19.9 ± 0.1

[a]From experiments at pH 7.4 and room temperature. [b]From kinetic studies of oxidation of K79G/M80X/F82C variants by $Fe(CN)_6^{3-}$. [c]From Az replacement experiments of K79G/M80X variants. Parameters $\Delta G^{\ddagger}$(X-C) and $\Delta G^{\ddagger}$(X) were calculated according to eq 5 from rate constants $k^{X\text{-}C}$ and k_{off}^{X}, respectively.

Switchable K79G/M80X/F82C Cyt *c* Variants. A series of K79G/M80X/F82C (X = Met, His, or Lys) variants with a Cys82 residue that can potentially ligate to the heme iron has been prepared. Spectroscopic, electrochemistry, and denaturation studies of these variants were used to establish the identity of the ligands to the ferric and ferrous heme iron as well as stability of ferric and ferrous proteins.

Ligands to the Heme Iron and Conformational Properties in Ferric K79G/M80X/F82C. The red-shifted Soret and Q-bands in K79G/M80X/F82C variants are consistent with those in other Cys/His-ligated heme proteins (Figure 5A and Table 1).[41] The presence of the characteristic thiolate-to-Fe(III) charge-transfer bands at ~635 and ~710 nm (Figure 5A) and the narrow spread of *g* values in the EPR spectra (Figure 5B) confirm the thiolate ligation to the ferric heme iron in these variants. Analyses of pH titration experiments under acidic conditions suggest a single transition from the low-spin Cys/His-ligated species to the high-spin heme species (Table 4). The pK_a values for this transition are lower than the apparent pK_a for acid-triggered unfolding of K79G[41] and suggest that Cys82 ligation to the ferric heme iron adds to the stability of ferric proteins. All three K79G/M80X/F82C variants exhibit two alkaline transitions (Figure S7 and Table 4). Studies of Met-ligated K79G and Cys78-ligated T78C/K79G have also observed two alkaline transitions for ferric proteins: of Met80 (K79G) or Cys78 (T78C/K79G) at the heme iron being replaced by a Lys residue, and of the Lys ligand being replaced by hydroxide, concomitant with partial protein unfolding.[41] Similar to T78C/K79G, the pK_a values for the Cys-to-Lys transition in K79G/M80X/F82C variants are much higher than the pK_a of 8.6 for the Met-to-Lys transition in K79G,[41] suggesting that Cys82 coordination to the ferric heme iron is favored over Lys, His, and hydroxide up to pH ~10.

Table 4. pK_a Values from Spectrophotometric pH Titrations and Proposed Ligand-Switching Processes of Ferric Cyt *c* Variants Studied or Referred to in This Work[a]

Variant	Alkaline		Acidic	
	pK_a	Proposed Ligand Switch	pK_a	Proposed Ligand Switch
K79G[b]	8.6 ± 0.1	Met80 → Lys	3.0 ± 0.1	Met80 → H_2O
	12.5 ± 0.1	Lys → OH^-	--	--
K79G/M80H	12.2 ± 0.1	His/Lys → OH^-	2.7 ± 0.1	His80 → H_2O
K79G/M80K*[b]	11.7 ± 0.1	Lys → OH^-	4.9 ± 0.2	Lys80 → H_2O
	--	--	3.3 ± 0.3	His18/H_2O → H_2O/ H_2O?
K79G/F82C	11.1 ± 0.1	Cys82 → His/Lys	2.7 ± 0.1	Cys82 → H_2O
	12.5 ± 0.1	His/Lys → OH^-	--	--
K79G/M80H/F82C	11.1 ± 0.2	Cys82 → His/Lys	2.4 ± 0.1	Cys82 → H_2O
	12.4 ± 0.1	His/Lys → OH^-	--	--
K79G/M80K*/F82C	11.3 ± 0.7	Cys82 → Lys	2.6 ± 0.1	Cys82 → H_2O
	12.5 ± 0.7	Lys → OH^-	--	--

[a]At room temperature. [b]From studies of Amacher *et al.* [41].

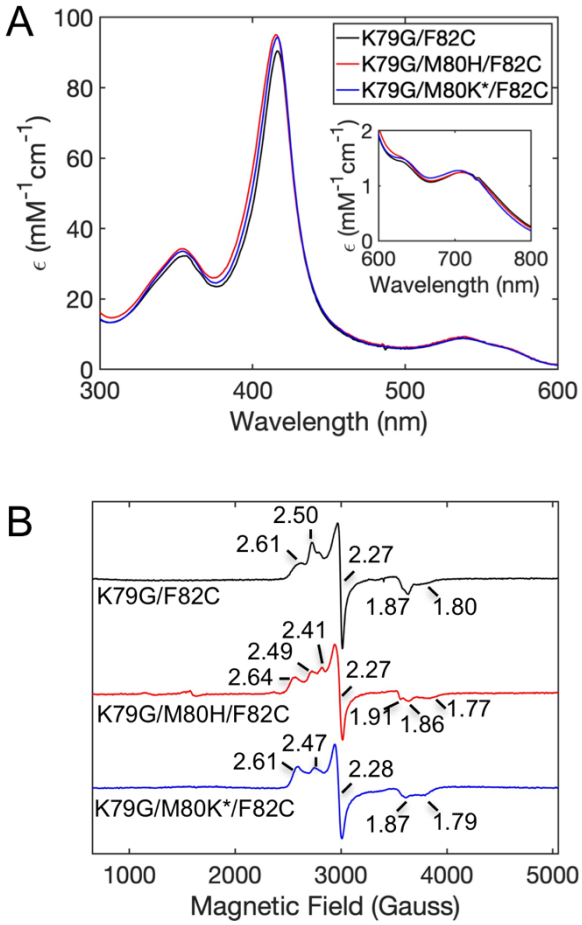

Figure 5. (A) Electronic absorption spectra at room temperature of ferric K79G/F82C (*black*), K79G/M80H/F82C (*red*), and K79G/M80K*/F82C (*blue*) in a 100 mM sodium phosphate buffer at pH 7.4. (*Inset*) the charge-transfer band region (600-800 nm) for the three proteins. (B) EPR spectra at 10 K of ferric variants in a 50 mM sodium phosphate buffer at pH 7.4.

The similarity of far-UV CD spectra to those of the parent K79G (Figure S8A) suggests that substitutions at residues 80 and 82 do not dramatically modify the secondary structure of the protein. The experimentally observed small decrease in the helical content in Cys-ligated K79G/F82C compared to that in Met-ligated K79G or Cys-ligated K79G/M80H/F82C and K79G/M80K*/F82C is also corroborated by the analyses of MD-derived models (Table S7 and Figure S9). Evidently, the Cys82-ligated K79G/F82C loses two short helices near Ω-loops C and D, but these helices are maintained in Cys82-ligated K79G/M80H/F82C and K79G/M80K*/F82C.

The deformation of the two helices in Cys82-ligated K79G/F82C is likely a result of Met80 positioned in the protein interior. In contrast, His80 and Lys80 in the other two variants are positioned on the protein surface, resulting in minimal perturbation of the polypeptide packing. Similar to these findings, only minor structural perturbations are observed in the crystal structure of WT* at high pH, when Met80 is no longer bound to the heme iron, but instead positioned on the protein surface.[89] Thus the expulsion of residue 80 from the heme pocket is associated with relatively small changes in the structure of cyt *c*. Global stabilities of all three Cys82-ligated variants from thermal denaturation studies are very similar (Figure S7B and Table S5, S6) and higher than that of the Met80-ligated K79G. Similar to findings with other Cys-ligated ferric proteins,[14,41] coordination of Cys82 to the ferric heme iron greatly increases the stability of cyt *c*.

Ligands to the Heme Iron and Conformational Properties in Ferrous K79G/M80X/F82C. Electronic absorption spectra of ferrous K79G/M80X/F82C variants are indicative of **6c** low-spin heme species (Table 1). The characteristic upfield signals in the ^{1}H NMR spectra (Figure 6A and 6C) establish that Met and Lys are ligand to the ferrous heme iron in K79G/F82C and K79G/M80K*/F82C, respectively. Based on our findings with K79G/M80H (Figure S3), it is not surprising that His-derived upfield ^{1}H signals are also not observed for K79G/M80H/F82C (Figure 6B). These findings suggest that the heme environment remains dynamic upon the addition of the F82C mutation to the parent K79G/M80H protein. Two very broad peaks at similar positions to those in the Lys-ligated ferrous species, at -2.2 ppm and -4.1 ppm, are noticeable in the spectra of K79G/M80H/F82C at pH 7.4 (Figure S3A). However, the relative intensities of these signals at pH 7.4 are much lower (<15%) than those at pH 10 (Figure S3A). We conclude that while both His- and Lys-ligated species are present for ferrous K79G/M80H/F82C at pH 7.4, the Lys-ligated species is only a minor component of this ensemble.

The effects of the added F82C substitution on the structure and dynamics of the differently-ligated ferrous variants were assessed with analyses of MD simulations. In all three K79G/M80X variants, the native Phe82 is buried (Figure S10). While the nonnative Cys82 is located in the protein interior in K79G/F82C, this residue becomes more solvent exposed in K79G/M80H/F82C and K70G/M80K*/F82C (Figures S9B and S10). The heat maps in Figure S11 compare contacts and their frequencies in K79G/M80X and K79G/M80X/F82C proteins. For the majority of contacts, the same contact pairs are found in K79G/M80X and corresponding K79G/M80X/F82C

proteins, suggesting preservation of the overall protein fold upon adding the F82C substitution. The changes upon adding the F82C substitution into K79G are minimal, except for the loss of contacts with residue 82 itself, with residues 64-66 and 73-75. In contrast, more contacts are perturbed upon adding the F82C substitution to K79G/M80H and K79G/M80K*, and these perturbations extend beyond residue 82 to Ω-loop C and the 60´s helix. In K79G/M80H/F82C, contacts of residue 82 with residue 64 that existed in K79G/M80H are lost but new contacts of residue 82 with residues 65 and 74 are formed. In addition, contacts between residues 46 and 81, 43 and 57, as well as between residues 49 and 56 disappear, but contacts of residue 77 with residues 46 and 47 are formed instead. For K79G/M80K*/F82C, contacts of residue 82 with residues 64-66 and 73-75 that existed in K79G/M80K* are largely lost, without new contacts formed. Further, contacts between residues 46 and 81, 49 and 81, 49 and 72, as well as between residues 46 and 67 are also lost.

There are also notable changes in contact frequencies, suggesting changes in conformational dynamics. A number of contacts have higher frequencies in K79G/M80H/F82C, compared to those in K79G/M80H. These changes as well as the new contacts that appear in K79G/M80H/F82C are consistent with structural rearrangement resulting from the F82C substitution in the His-ligated protein. In contrast, the loss of several contacts and also the decrease in frequency of multiple remaining contacts in K79G/M80K*/F82C, compared to those in K79G/M80K* suggest that the Lys-ligated protein becomes more disordered.

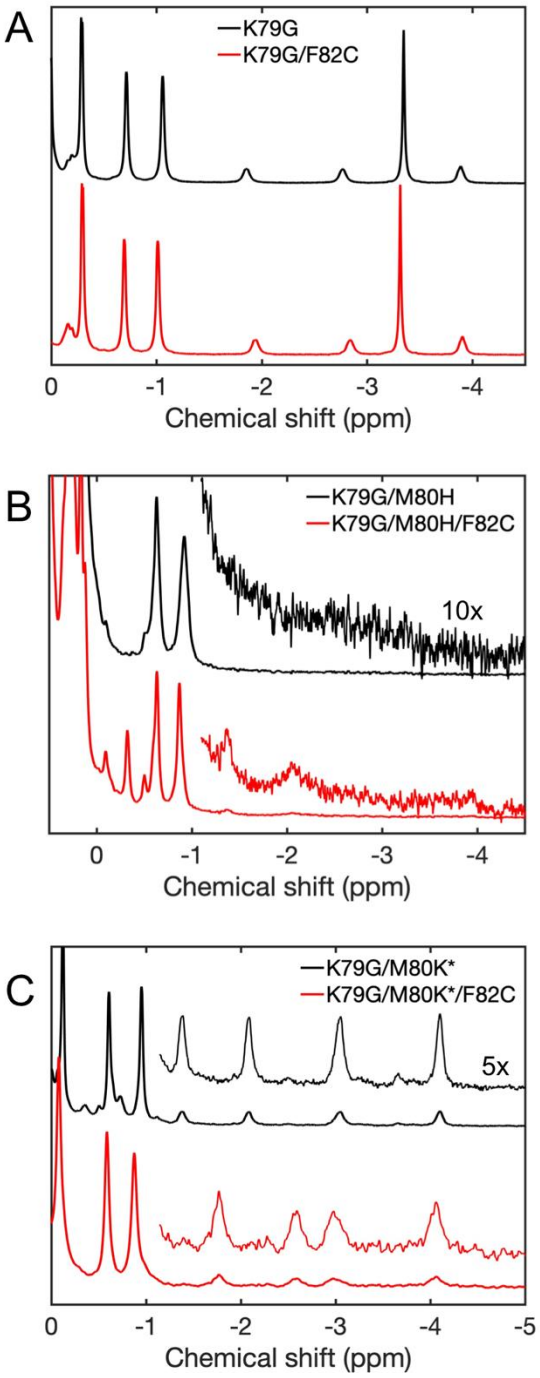

Figure 6. The upfield region of the ^{1}H NMR spectra for ferrous (A) K79G and K79G/F82C, (B) K79G/M80H and K79G/M80H/F82C, and (C) K79G/M80K* and K79G/M80K*/F82C cyt *c* variants.

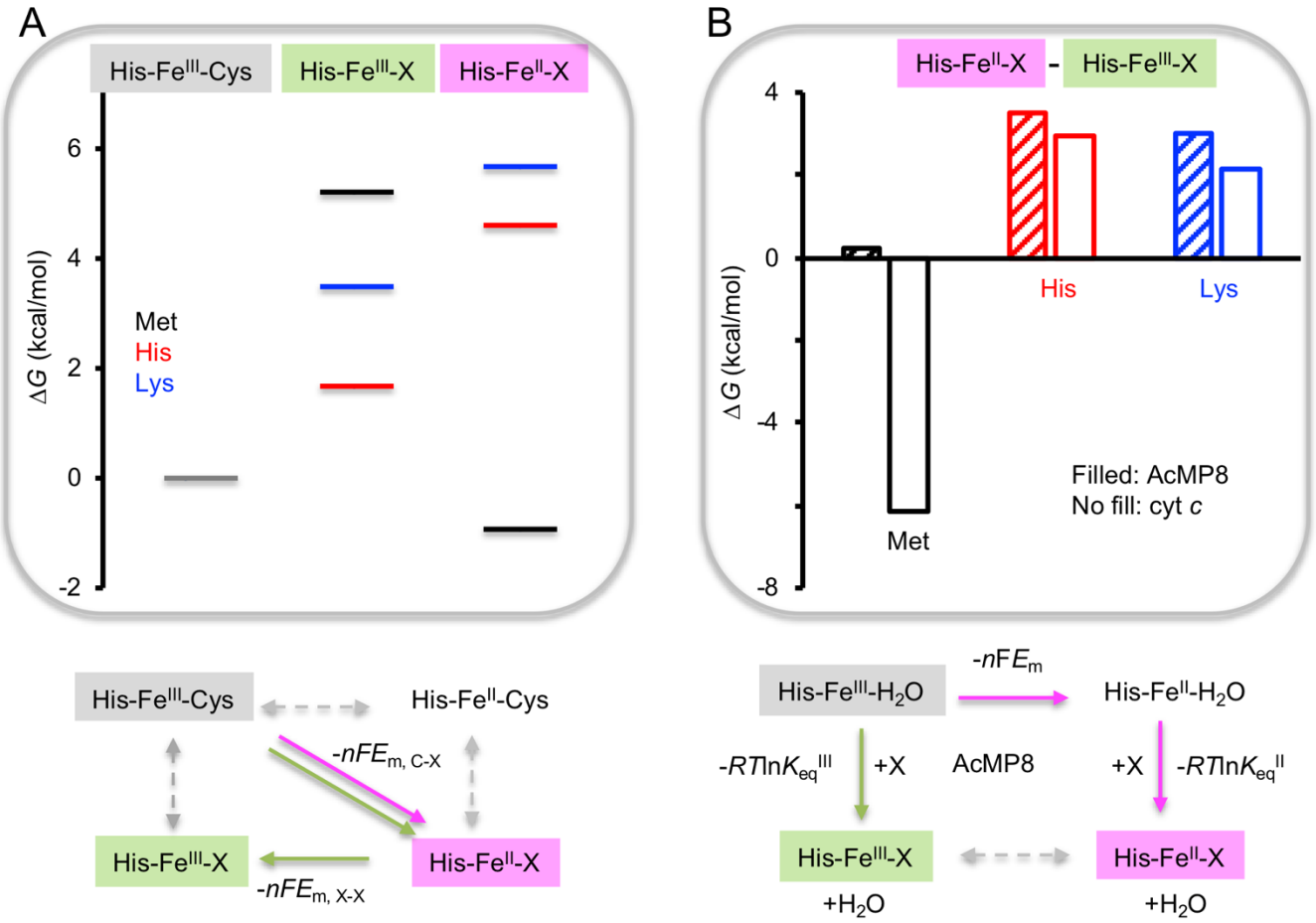

Figure 7. (A) (*Top*) Relative energy levels of ferric and ferrous cyt *c* variants. (*Bottom*) A scheme illustrating the derivation of these values. The free energy of the His-Fe^{III}-Cys species was set to zero to serve as a reference for all other energy levels. Reduction potentials of the K79G/M80X/F82C variants (Table S4) were used to calculate free energies of the His-Fe^{II}-X species. Free energies of the His-Fe^{III}-X species relative to those of the His-Fe^{II}-X species were calculated using reduction potentials of K79G/M80X variants (Table S4). (B) (*Top*) Changes in free energy for AcMP8 adducts and cyt *c* variants upon reduction of the heme iron. (*Bottom*) A scheme illustrating the derivation of these values. The reduction potential E_m of -139 mV[90] for the His-Fe-H_2O species was from cyclic voltammetry measurements. Equilibrium constants K_{eq} were calculated from experimental binding affinities K_a[5,41] using $K_{eq}=[H_2O]\times K_a$ with $[H_2O]$ = 55.5 M.

Reduction Potentials and Redox-Dependent Stability of K79G/M80X/F82C. Spectroelectrochemistry measurements of K79G/M80X/F82C were performed in both the

reductive and oxidative directions (Figure S12), and the reduction potentials are summarized in Table S4. As in other studies of proteins that experience redox-dependent changes in ligation to the metal ion,[91-92] a hysteresis, with different potential values from titrations in the reductive and oxidative direction, was observed for K79G/M80K*/F82C. Slow kinetics of ligand-substitution reactions have been suggested as a possible origin for the observed hysteresis.[8] A hysteresis was not observed for K79G/F82C and K79G/M80H/F82C variants, suggesting that ligand-substitution reactions in these proteins are fast relative to the timescale of spectroelectrochemistry measurements.

The redox-dependent protein stability was analyzed using eq 8 relating the difference in the Gibbs free energy of ferric ($G°(Fe^{III}\text{-C})$) and ferrous ($G°(Fe^{II}\text{-X})$) states to the reduction potential ΔE(C-X). Given the same coordination sphere and similar global stability of the three Cys82 variants with Fe^{III}-C ligation (Figure S8B and Table S6), we assume that their free energy levels are similar and set them to be zero in order to map the relative energies of other ferrous conformers. Analyses of reduction potentials in Table S4 suggests that the Met-ligated ferrous K79G/F82C has the lowest energy, about 5.5 kcal/mol lower than the His-ligated ferrous K79G/M80H/F82C. The Lys-ligated ferrous K79G/M80K*/F82C is the least stable (Figure 7A and S13A). Thermal denaturation measurements of these differently-ligated ferrous variants (Figure S13B) have revealed the same trend as that from measurements of reduction potentials.

$$G°(Fe^{II}\text{-X})-G°(Fe^{III}\text{-C}) = -nF\Delta E(\text{C-X}) \qquad \text{(eq 8)}$$

Kinetics of Redox-linked Ligand Switch in K79G/M80X/F82C. Our studies of oxidation reactions of ferrous T78C/K79G by $Fe(CN)_6^{3-}$ and $Co(phen)_3^{3+}$ have established that in that previously characterized variant ET takes place first and is followed by the Met-to-Cys ligand switch.[26] With $Fe(CN)_6^{3-}$, the ET step is fast and finished within the instrument dead-time, facilitating characterization of the ligand-switching process and associated reaction intermediates. For K79G/F82C in this work, the Fe^{III}-Met intermediate, readily distinguished by the characteristic charge-transfer band with λ_{max} =695 nm (Figure 8A), confirms the two-step reaction mechanism of fast ET followed by ligand switch also takes place in this new variant. The λ_{max} of the charge-transfer absorption band gradually shifts to ~710 nm and increases in intensity. The time course of the absorbance at 712 nm (Figure 8B) is best fit to a biexponential equation, yielding two rate constants of 34 s^{-1} and 5.2 s^{-1}. The slow phase, at approximately 11% amplitude, has been

previously assigned to the Met80-to-Lys73 ligand switch of the minor species having oxidized Cys.[26]

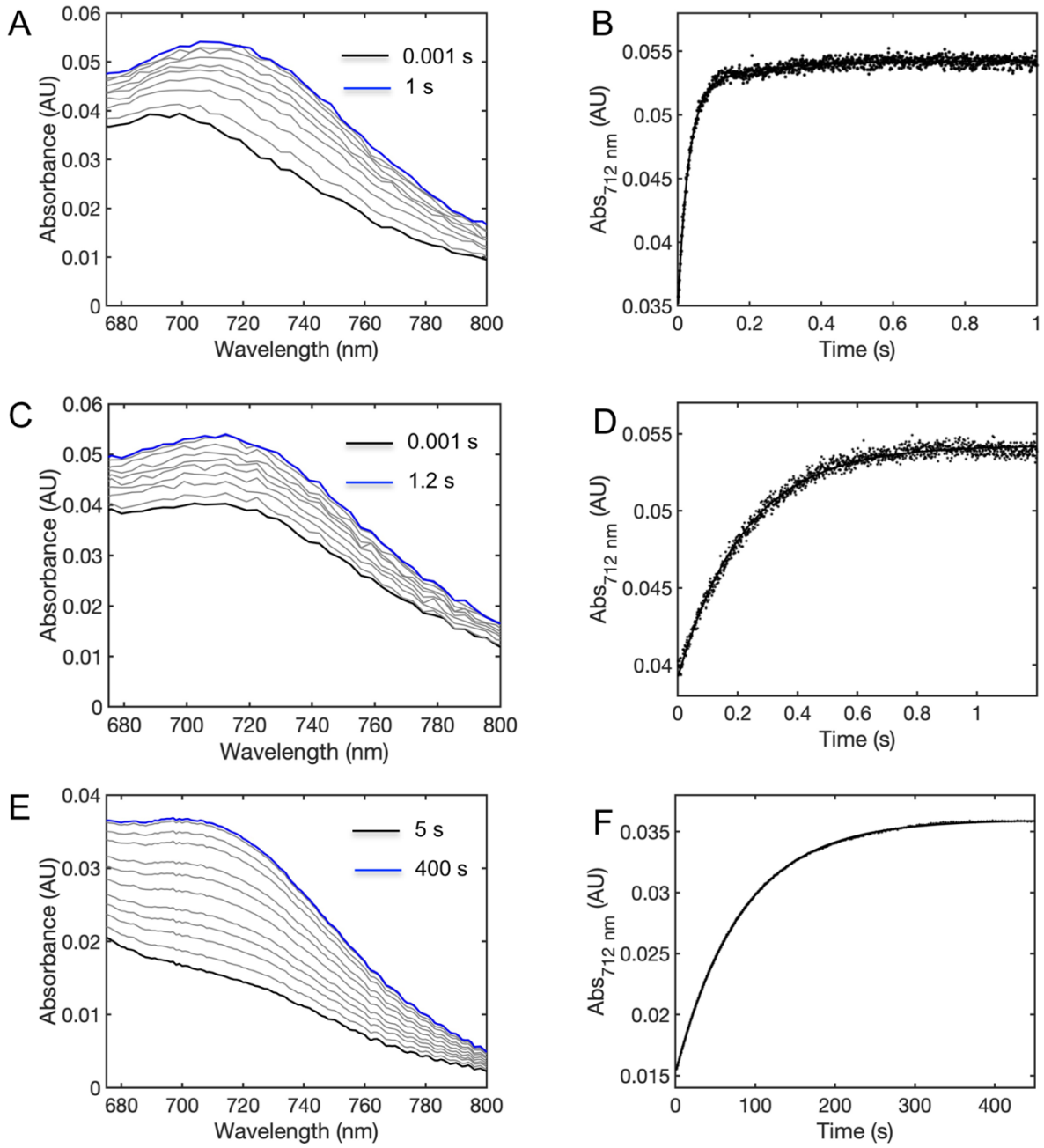

Figure 8. Spectral changes in the charge-transfer band region (675-800 nm) (*left*) and the corresponding time course of the absorbance at 712 nm (*right*) for oxidation of ferrous K79G/F82C (A and B), K79G/M80H/F82C (C and D), and K79G/M80K*/F82C (E and F) by $Fe(CN)_6^{3-}$ at room temperature. The final concentrations of $Fe(CN)_6^{3-}$ in these experiments were 1.5 mM. The final concentrations of the proteins were about 45 μM, 50 μM, and 35 μM for K79G/F82C,

K79G/M80H/F82C, and K79G/M80K*/F82C, respectively. The time dependence of K79G/F82C in panel B was fit to a biexponential equation, yielding two rate constants of $k^{M\text{-}C} = 34.0 \pm 1.4\ s^{-1}$ and $k^{M\text{-}K73} = 5.2 \pm 0.5\ s^{-1}$. The slow phase, exhibiting ~11% amplitude, is likely from the Met80-to-Lys73 ligand-switching process in the minor species having oxidized Cys82, as in our previous study on T78C/K79G.[26] The time courses for K79G/M80H/F82C (panel D) and K79G/M80K*/F82C (panel F) were fit to monoexponential equations, yielding $k^{H\text{-}C} = 4.4 \pm 0.2\ s^{-1}$ and $k^{K\text{-}C} = 0.012 \pm 0.001\ s^{-1}$, respectively. The minor species with oxidized Cys82 may exist in these proteins as well, however, His and Lys dissociation steps are slow in these variants, and therefore the kinetics for the X-to-Lys73 switch were not possible to separate from those for the X-to-Cys switches.

Unlike the Met-ligated ferric hemes, the His- and Lys-ligated ferric hemes do not exhibit distinct absorption signals to monitor their population directly and instead only the build-up of the ~710 nm absorbance (Figure 8C, 8E), characteristic of the Fe^{III}-Cys species, was observed for K79G/M80H/F82C and K79G/M80K*/F82C. The time course of the absorbance at 712 nm (Figure 8D, 8F) was fit to a monoexponential equation, yielding $k_{obs}^{X\text{-}C}$ values of $4.4\ s^{-1}$ and $0.012\ s^{-1}$ for K79G/M80H/F82C and K79G/M80K*/F82C, respectively. The minor species with oxidized Cys82 may exist in K79G/M80H/F82C and K79G/M80K*/F82C as well. Instead of being limited by the approach of Lys73 to the heme as in K79G/F82C (the dissociation of Met80 is fast),[26] however, the switch to the Lys73 coordination in these variants is limited by the slow dissociation of His80 and Lys80 and thus its kinetics are not separable from those of the switch to the Cys82 coordination.

In contrast to $Fe(CN)_6^{3-}$, $Co(phen)_3^{3+}$ does not interfere with measurements of the heme absorption changes in the Soret spectral region. The ET step is slower with this latter oxidant and is detected in the data from stopped-flow measurements. With the observable ET step in the $Co(phen)_3^{3+}$ reactions, triexponential (K79G/F82C) and biexponential (K79G/M80H/F82C and K79G/M80K*/F82C) equations were used to fit time courses of absorbance changes of these kinetics. A distinct red-shifted Soret band of the Cys-ligated species (6-10 nm Table 1) is easily distinguished from the Met-, His- and Lys-ligated species in the spectra. Therefore, the intermediate Fe^{III}-X species is readily observed (Figure 9). By monitoring disappearance of this

transient species, one can then conveniently determine X-to-C ligand-switching kinetics. The rate constants for the ligand-switching step were the same in measurements monitoring changes in either the Soret or near-IR spectral regions. Therefore, to reduce protein consumption, subsequent studies of the temperature and pH-dependence of the reaction kinetics monitored absorbance changes just in the Soret region.

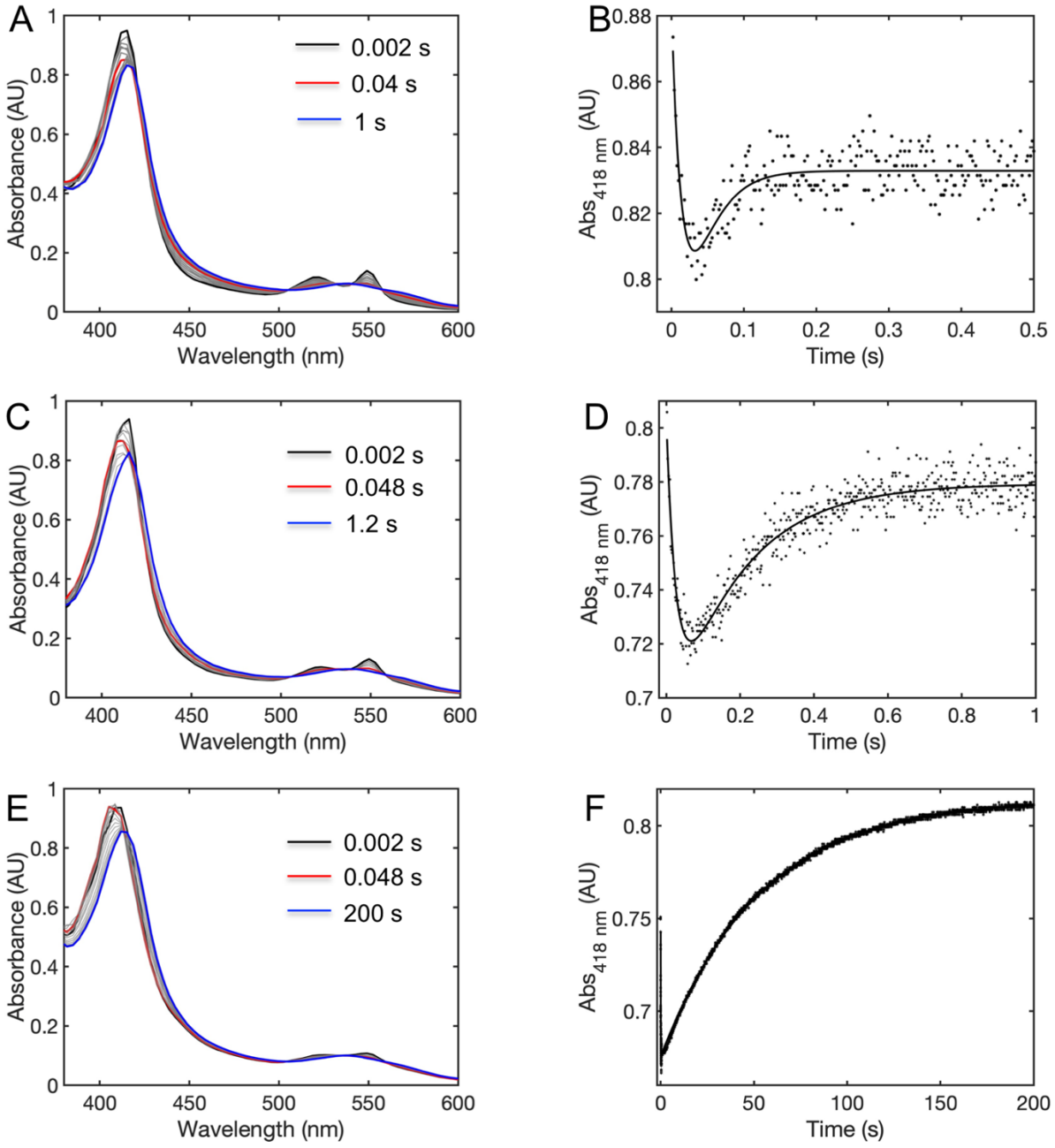

Figure 9. Spectral changes in the 380-600 nm range (*left*) and the corresponding time courses of the absorbance at 418 nm (*right*) for oxidation of ferrous K79G/F82C (A and B), K79G/M80H/F82C (C and D), and K79G/M80K*/F82C (E and F) by $Co(phen)_3^{3+}$ in a 10 mM sodium phosphate buffer at pH 7.4 containing 100 mM NaCl at room temperature. The protein concentration was about 8 μM. The final concentrations of $Co(phen)_3^{3+}$ were 0.34 mM, 0.1 mM, and 0.1 mM for K79G/F82C, K79G/M80H/F82C, and K79G/M80K*/F82C, respectively. Both ET and the X-to-Cys ligand-switching processes were captured under these experimental conditions. The solid lines are fits to a biexponential equation.

Temperature Dependence of Ligand-Switching Kinetics for K79G/M80X/F82C. Kinetics of oxidation of switchable K79G/M80X/F82C were examined in the temperature range from 15 to 35 °C to determine enthalpic and entropic contributions to the activation of associated redox-linked ligand-switching processes. The Eyring plots[93] for the ligand-switching steps are linear for all three variants (Figure 10). Activation parameters $\Delta H^{\ddagger}$(X-C), $\Delta S^{\ddagger}$(X-C), and $\Delta G^{\ddagger}$(X-C) from fits of these dependencies are listed in Table 5. The trend in the $\Delta G^{\ddagger}$(X-C) values for ligand substitution from these studies is Lys > His ≈ Met, again revealing the greatest activation barrier for replacement of Lys.

The $\Delta H^{\ddagger}$ value for the switch of Lys to Cys is about 10 kcal/mol lower than the values for His and Met. Among Lys, His and Met ligands, only the dissociation of Lys at pH 7.4 is accompanied by a protonation step. At pH 10, when 24% of the population of the uncoordinated Lys is expected to be neutral (pK_a=10.5),[77] the Eyring plot deviates from linearity (Figure S14), suggesting that the mechanism of redox-linked ligand switch under these conditions may be more complicated, potentially because of partial unfolding of the protein at higher temperatures and alkaline pH. Although these experimental challenges prevent quantitative determination of the effect of Lys protonation in our system, the observed increase in the $\Delta H^{\ddagger}$(X-C) value at higher pH is qualitatively consistent with the role of Lys protonation in the Lys-to-Cys ligand-switching process. The activation parameters for Lys protonation were not available and instead we used thermodynamic values[77] to approximate possible effects of protonation on Lys dissociation. After subtracting the literature $\Delta H°$ value of -11.6 kcal/mol[77] for Lys protonation from the experimental $\Delta H^{\ddagger}$(X-C) value for K79G/M80K*/F82C at pH 7.4, $\Delta H^{\ddagger}$(X-C) values for all three variants become

similar (Table 5). After subtracting the $\Delta S°$ value of 9 cal/mol/K for Lys protonation[77] from the $\Delta S^{‡}$(X-C) value for K79G/M80K*/F82C, the trend in the $\Delta S^{‡}$(X-C) values is Met > His > Lys.

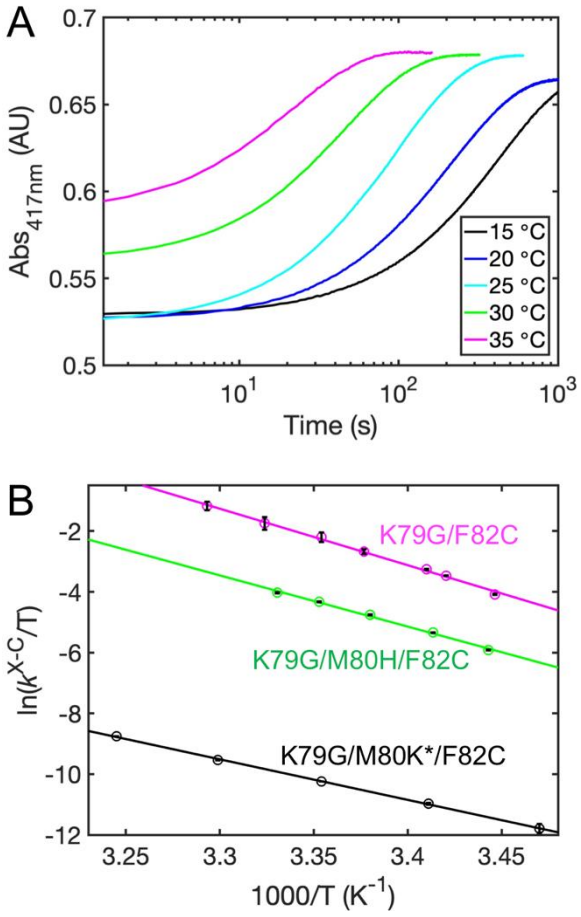

Figure 10. (A) Time courses of absorbance at 417 nm for oxidation of K79G/M80K*/F82C by 0.2 mM $Co(phen)_3^{3+}$ at various temperatures at pH 7.4. (B) Eyring plots of $\ln(k^{X\text{-}C}/T)$ versus 1000/T for the three K79G/M80X/F82C variants. Fits of the data in panel B to eq 6 yielded $\Delta H^{‡}$(X-C) and $\Delta S^{‡}$(X-C) parameters in Table 5.

Table 5. Activation Parameters for the X-to-Cys Ligand-Switching Processes in K79G/M80X/F82C Cyt *c* Variants[a] and for Ligand X Dissociation in Related Proteins

Ligand X	Variant	$\Delta H^{\ddagger}$ (kcal/mol)	$\Delta S^{\ddagger}$ (cal/mol/K)	$-T\Delta S^{\ddagger}$ (kcal/mol)	$\Delta G^{\ddagger}$ (kcal/mol)
His	K79G/M80H/F82C[b]	33.39 ± 0.81	56.08 ± 2.74	-16.71 ± 0.82	16.68 ± 1.15
	Im-Fe^{III}-TPP[94]	17-20	15-19	N/A[c]	N/A[c]
	hh cyt *c*, unfolded[95]	21.6 ± 0.5	24 ± 2	-7.15	14.45
	hh cyt *c*, partially folded[d]	16.67	6.82	-2.03	14.64
Lys	K79G/M80K*/F82C[b]	26.53 ± 0.97	21.44 ± 3.32	-6.39 ± 0.99	20.14 ± 1.39
	K79G/M80K*/F82C[b], pH 10	78.4	186.7	-55.6	22.8
	hh cyt *c*, k_b	35.55 ± 0.89	55.28 ± 3.02	-16.47 ± 0.90	19.07 ± 1.27
	hh cyt *c*, k_b[e,f]	14.6 ± 4.3	-15.5 ± 14.6	4.6 ± 4.4	19.2 ± 6.1
Met	K79G/F82C[b]	37.01± 1.30	72.40 ± 4.37	-21.58 ± 1.30	15.44 ± 1.84
	cyt c_2[g]	21.76	21.14	-6.30	15.46
	hh cyt *c*, k_f[e]	27.9 ± 6.8	38.7 ± 23.0	-11.5 ± 6.9	16.3 ± 9.6

[a]At pH 7.4, unless specified otherwise. [b]From Eyring plots using $k^{X\text{-}C}$ values from ligand-switching experiments. [c]Not available. [d]From our fits of digitized *k* and *T* values for the slow phase in Figure 3A from studies of Colon *et al.*[96] to eq 6. [e]From our fits of *k* and *T* values in Table IV from studies of Davis *et al.*[49] to eq 6. [f]Experiments were performed at only three temperatures. [g]From our fits of k_{12} and *T* data in Table III from studies of Dumortier *et al.*[97] to eq 6.

Temperature Dependence of the Alkaline Transition in Horse Heart Cyt *c*. The alkaline transition in cyt *c* is the replacement of the native Met80 ligand by a nearby Lys73 or Lys79 at the heme iron at alkaline pH (Scheme 2). The temperature dependence of rate constants for both forward Met-to-Lys (k_f) and back Lys-to-Met (k_b) reactions in *hh* cyt *c* has been previously examined by studying the transition at three temperatures (16, 21 and 25 °C).[49] We performed the Eyring analyses of the rate constants k_b from this earlier work to derive $\Delta H^{\ddagger}$ = 14.6 ± 4.3 kcal/mol and $\Delta S^{\ddagger}$ = -15.5 ± 14.6 cal/mol/K for the back reaction. Considering large error bounds and a surprising negative value of $\Delta S^{\ddagger}$, we decided to extend the temperature range to allow for informative comparison of Lys dissociation kinetics in alkaline cyt *c* conformers to our Lys dissociation kinetics from studies of thiolate variants. We carried out the downward pH jump experiments (from initial pH 10 to final pH 7 or 7.5) with *hh* cyt *c* at seven different temperatures within a broader temperature range of 16-32 °C. The observed rate constants (k_{obs}^{pH}) from our work agree with those from earlier studies. With addition of new data points from our experiments, the Eyring plot of the composite data set (Figure S14) yielded $\Delta H^{\ddagger}$ = 35.6 ± 0.9 kcal/mol and $\Delta S^{\ddagger}$ = 55.3 ± 3.0 cal/mol/K, respectively. The error bounds of these activation parameters are smaller than those from fits of the earlier data,[49] and the $\Delta S^{\ddagger}$ value for k_b is now unambiguously positive.

DISCUSSION

Metal-Ligand Interactions and Protein Stability. Multiple factors, including ligands at the metal center, oxidation state of the metal center, solvation, and interactions within the polypeptide scaffold, influence protein stability, and these factors are not always easy to separate. By modifying a single ligating residue X in the protein series and complementing analyses with DFT calculations and MD simulations, distinct thermodynamic contributions of each of the three ligands Met, His, and Lys, as well as the role of the surrounding polypeptide, can be evaluated.

Our DFT calculations suggest that ligand X' loss from the ferric heme iron becomes more unfavorable for $(CH_3)_2S$ < Im < CH_3NH_2. Despite employing different model compounds and calculation methods, the differences in the gas-phase ΔG values for ligand loss between the thioether and Im species are very similar to those in the study of Solomon and coworkers.[98] Further, we also find a ruffling of the thioether-ligated ferric heme (Table S2), consistent with the greater covalency of the Fe^{III}-S bond. The earlier study has attributed the stronger Fe^{III}-N(Im) bond to a larger Δ,[98] the difference in energy between the metal and the ligand orbitals and also argued that

the trend can be rationalized by the fact that N is more electronegative than S or using hard-soft acid base formalism. The hardness of a ligand can be quantified using the difference in energies of LUMO and HOMO orbitals,[99] and we find the trend from such calculations (Figure 3B) that agrees with the calculated ΔG energies of ligand loss in our DFT study or experimental ΔG energies of activation from ligand dissociation kinetics of protein variants. The lower basicity and nucleophilicity of Im compared to that of amine has been attributed to larger reorganization energy upon electrophilic attack on the nitrogen,[100] and these arguments could be further extended to bond formation with metal ions such as ferric iron.

The trend in free energy of ligand dissociation $(CH_3)_2S$ < Im < CH_3NH_2 is maintained when solvation energy is taken into account, however, the relative energy differences do change (Figure 3A). The distinct solvation energy of the released X′ appears to be the main contributor to the difference in the solvation energy for the dissociation (Table S1). This finding highlights an important role of solvation in the ligand dissociation process.

The stability trend Met < Lys < His for the protein Fe^{III}-X species (Figure 7A) differs from the trend in free energies of individual **6c** model complexes (Table S1) and resembles more the one in binding affinities of **6c** Im-Fe^{III}-H_2O for X′ and of acetylated microperoxidase 8 (AcMP8) for X and X mimics (Figure S1),[5,14,22,101] with interactions of the ferric heme iron with thioether of Met being the least favored. This finding highlights the important role of the protein-derived ligand in both metal-bound and unbound state in tuning overall stability of metalloproteins. Our MD simulations suggest that heme in the Fe^{III}-Met cyt *c* species is well-protected from the solvent (Figures S15 and S16). The SASA value for the heme in the Lys-ligated ferric K79G/M80K* is similar with that in the Met-ligated ferric K79G, but there are larger fluctuations in these parameters for the Fe^{III}-Lys cyt *c* species. The heme in the Fe^{III}-His cyt *c* species is the most exposed.

Stabilities of Fe^{II}-X protein species reveal the following trend Lys < His < Met (Table S4 and S6). This trend deviates from the one for the Fe^{III}-X protein species, suggesting redox-dependent differences in stabilization by the protein scaffold. Ultrafast X-ray spectroscopy studies of ferrous Met-ligated wild-type cyt *c* revealed that protein constraints add about 4 kcal/mol to the weak Fe-S(Met) bond, and the dominant contribution to this stabilization was attributed to the –OH group of Tyr67[102], which forms a hydrogen-bonding network that encompasses Met80, a bound H_2O

molecule, Asn52, and Thr78.[50] Our MD-derived models revealed that the hydrogen-bonding network involving Met80 is largely unperturbed in ferrous Met-ligated K79G and K79G/F82C (Figure S17), suggesting that, similar to the wild-type protein, the Fe^{II}-Met80 species in these variants is likely stabilized by intramolecular interactions involving the ligand. The hydrogen-bonding network in K79G/M80K* is largely intact, but the F82C mutation in K79G/M80K*/F82C abolishes interactions between Asn52 and Thr78 by pushing these two residues away from each other. The network involving His80 in ferrous K79G/M80H and K79G/M80H/F82C shows the greatest number of dynamic contacts, suggesting less stabilization from this protein network for the Fe^{II}-His80 cyt *c* species.

Despite similar number and frequency of contacts within the ligand-mediated hydrogen-bonding network, ferrous K79G/M80K* is less stable than ferrous K79G (Figure 7A and Table S6). It is possible that the properties of Lys80 and Met80 in the unfolded protein differentiate the stabilities of K79G/M80K* and K79G. The free energy of Lys solvation is ~8 kcal/mol more than that of Met.[103] The stabilization from protonation and solvent exposure of Lys80 in the unfolded K79G/M80K* may dampen the stabilization effect of the Lys-iron coordination and interactions provided by the polypeptide in the folded protein.

Our stability findings (Figure 7A) reveal that reduction of the heme iron *increases* the free energy of the His- and Lys-ligated proteins by 2-3 kcal/mol but *decreases* the free energy of the Met-ligated protein by about 6 kcal/mol. While His- and Lys-ligated heme species in cyt *c* mirror redox-dependent stability trends of the corresponding AcMP8 adducts,[5,41] the Met-ligated heme iron species exhibit different trends when enclosed in the protein frame in cyt *c* and largely exposed to the solvent in AcMP8 (Figure 7B). Comparisons of the MD-derived models offer structural insights to these effects, most importantly suggesting the role of the ligand-mediated hydrogen-bonding network in stabilizing the Met-ligated ferrous species. As previously argued,[5] exclusion of the solvent in the folded protein differentially affect the stability of ferric and ferrous species, particularly in the case of cyt *c*, which has a relatively hydrophobic Met80 ligand and a tightly-enclosed heme. Among the differently-ligated protein variants in this work, Met80-ligated K79G has the lowest SASA value for the heme group (Figure S15C), consistent with these explanations. Larger fluctuations in these parameters are observed for K79G/M80K* and K79G/M80H, suggesting a more open heme crevice in these variants.

Differentiating between the Heme Crevice Opening and Bond Breaking. Dissociation of ligand from the ferric iron has been traditionally examined with exogenous small molecules, such as Az, cyanide, imidazole, and pyridine and its derivatives.[15,104] Among them, Az has been particularly popular because of its small size and high binding affinity; and several Az binding studies have been performed with cyt *c* variants from different organisms.[15,30,104-105] These prior studies and work with other **6c** ferric heme proteins have concluded that the protein-derived axial ligand has to dissociate prior to Az binding the heme iron.[15] The rate-limiting step for formation of the "open" conformer (described by the rate constant k_{off}^{X} in Scheme 1) is sensitive to mutational perturbations both near and remote from the heme,[30,105-107] thus, protein dynamics could affect these kinetics.

A number of studies, including a seminal report of ligand substitution triggered by addition of several different small ligands to *hh* cyt *c*,[15] suggest that the observed rate-limiting step in Met-ligated cyt *c* proteins is opening of the heme crevice (Scheme 1). Mauk and coworkers have systematically examined thermodynamic and kinetic effects of Phe82X (X=Gly, Ser, Tyr, Leu, and Ile) mutations in yeast *iso*-1 cyt *c* on the alkaline transition (Met-to-Lys ligand substation at the heme iron at alkaline pH) and concluded a critical role of Phe82 in stabilizing the native Met80 ligation to the heme iron.[30,108] Similarly, studies of Im binding to variants of a structurally similar protein cyt c_2 revealed that the rate-limiting step in this reaction is the rearrangement of the hinge region near the heme, which is analogous to Ω-loop D of cyt *c*.[109-110] Polypeptide dynamics are important in ligand dissociation in these proteins. However, one could argue that in principle, when steric hindrance around the heme is minimal or the barrier for the Fe^{III}-X bond breaking is particularly high, the rate of ligand dissociation will be governed by this latter process. The side-by-side comparison of ligand-substitution kinetics in our protein variants having the same polypeptide scaffold but different axial ligands X allows for evaluation of the interplay of the intrinsic dynamics of the heme crevice and the Fe^{III}-X bond breaking (Scheme 3), as well as their timescales.

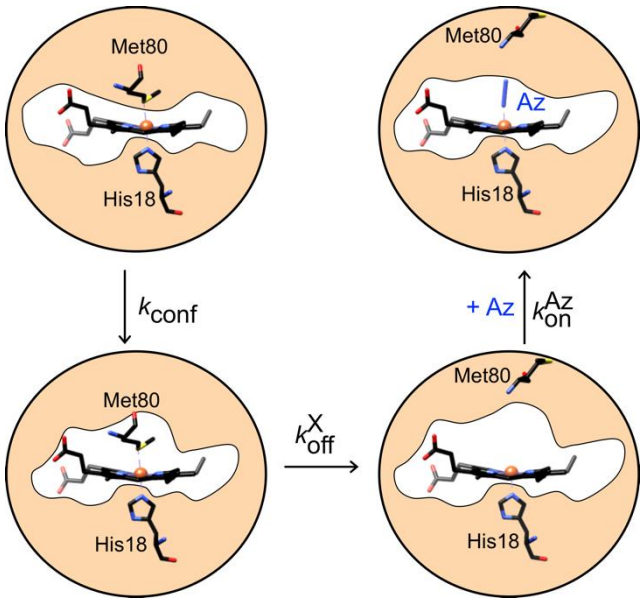

Scheme 3. Proposed reaction scheme for the ligand X dissociation from the heme iron center followed by Az binding.

$$k_{obs}^{X} = \frac{k_{conf} \times k_{off}^{X}}{k_{conf} + k_{off}^{X}} \qquad \text{(eq 9)}$$

The similar values of rate constants k_{off}^{X} and $k^{X\text{-}C}$ in Az binding and X-to-Cys switching experiments, respectively, of His- and Lys-ligated variants suggest that the same process is being probed in these two ligand-substitution experiments. The finding that the values of these rate constants for the Lys-ligated variant (Table 3) are *much smaller* (>600 fold) than those of known rate constants (6-360 s^{-1}) for heme crevice opening in cyt *c*, [30,105-107] suggests that these rate constants report kinetics of the Fe^{III}-N(Lys) bond breaking. Supporting this conclusion, values of a similar magnitude (0.016-0.78 s^{-1}) have been reported for Lys dissociation in cyt *c* variants with Lys at different locations or different heme environment.[22,26,37,44,88,108]

For His-ligated variants the k_{off}^{H} and $k^{H\text{-}C}$ values (4.4±0.2 s^{-1}) are lower than the values associated with heme crevice opening in Met-ligated cyt *c* proteins. Kinetics of His dissociation from the heme iron have been previously reported for a number of cyt *c* variants, having His residues at different locations and mutations at nearby sites. The wide range of rate constants in partially unfolded conformers at equilibrium or during cyt *c* refolding (from 0.7 to 30 s^{-1}) illustrate the important role of the protein environment in governing the His dissociation process. [95-96,111-113] The finding that rate constants for His dissociation range from 25 to 150 s^{-1} even in fully denatured

proteins suggest that the local amino-acid sequence also affect His dissociation rates.[114] It is thus possible that the rate constant in our studies reports on the Fe^{III}-N(His) bond-breaking process, but, because this process and heme crevice opening occur on a similar timescale, the observed rate constant k_{obs}^{H} may be the composite of the rate constants k_{off}^{H} and k_{conf} (eq 9).

In contrast to His- and Lys-ligated variants, rate constants for Met-ligated K79G (k_{off}^{M}=92 s^{-1}, from Az binding experiments) and K79G/F82C ($k^{M\text{-}C}$ =34 s^{-1}, from X-to-Cys switching experiments) are different. We have previously found that deprotonation of the incoming Cys78 is the rate-limiting step in the Met-to-Cys ligand switch in T78C/K79G.[26] For T78C/K79G, the rate constant for the Met-to-Cys ligand switch $k^{M\text{-}C}$ is 18.6±0.3 s^{-1} at pH 7.4 and becomes faster (~35 s^{-1}) at pH>9, when Cys78 is deprotonated in the ferrous protein (pK_a = 7.9±0.7). In contrast, the rate constant for the Met-to-Cys ligand switch $k^{M\text{-}C}$ in K79G/F82C does not change in the pH range 6 to 9. This finding, together with lower rate constants for the His-to-Cys (4.4±0.2 s^{-1}) and Lys-to-Cys (0.012±0.001 s^{-1}) ligand-switching processes, suggest that Cys82 deprotonation is not the rate-limiting step for any of the three switchable X variants in this study.

The value of k_{off}^{M} from Az binding experiments with non-switchable K79G is the same as the value found with Im.[88] Kinetics of Fe^{III}-S(Met) bond breaking have not yet been determined directly but other experiments allow for estimates of this value. Photolysis of NO-bound ferric cyt *c* has revealed that Met rebinding occurs about 3 μs ahead of NO binding, and the k_{obs}^{NO} values for bimolecular process of NO binding are 455 s^{-1} and 4348 s^{-1} at NO concentrations of 0.24 mM and 2.4 mM, respectively.[79] With these two points as entries for the dependence of k_{obs}^{NO} on NO concentration, it could be extrapolated that k_{obs}^{NO} reaches a plateau at approximately 9×10^4 s^{-1}, presumably the value for Fe^{III}-S(Met) bond breaking. Another estimate for the rate constant of Fe^{III}-S(Met) bond breaking can be made from the $\Delta G^{\ddagger}$(M) barrier calculated using the theoretical energy difference between the amine- and thioether-ligated species from our DFT calculations (10.7 kcal/mol, Table S1 and Figure 3A) and the experimental value for the Fe^{III}-N(Lys) bond breaking in K79G/M80K* (19.9 kcal/mol, Table 3). These calculations yield the rate constant for Fe^{III}-S(Met) bond breaking of approximately 2×10^5 s^{-1}, very close to the estimated value from NO photolysis studies. Finally, if we use K_d of 0.38 M for AcMet binding to ferric AcMP8[5] and assume that ligand binding in this simple model system, which is not complicated by heme crevice

opening, is controlled by diffusion of the two molecules (k_{on}^{M} = ~10^8 $M^{-1}s^{-1}$), we obtain the k_{off}^{M} value of 3.8×10^7 s^{-1}. These rough calculations suggest that the magnitude of 10^5 s^{-1} that we project for the rate constant of Fe^{III}-S(Met) bond breaking in cyt *c* is not unreasonable.

The k_{off}^{M} values of 6-360 s^{-1} for different Met-ligated cyt *c* proteins,[15,30,105-107] are much smaller than our estimates of ~$0.9\text{-}2\times10^5$ s^{-1} for the rate constant of Fe^{III}-S(Met) bond breaking. While the polypeptide scaffold is certainly known to tune ligand-dissociation kinetics, it is unlikely that it could slow down this process by multiple orders of magnitude in this particular case. As shown by Solomon and coworkers, the protein scaffold in a more stable ferrocyt *c* strengthens the Fe^{II}-S(Met) bond by only 4 kcal/mol; they attributed this stabilization to the hydrogen-bonding network involving Met80 (Figure S17). The hydrogen bond to Met80 is not formed in the ferric protein and the stability of the ferric protein is 6 kcal/mol less than that of the ferrous protein (Table S4), despite the intrinsically stronger Fe^{III}-S(Met) bond[102], so the effect of the protein scaffold may be more modest in this case. We therefore suggest that, as in other Met-ligated cyt *c* variants,[15,30,105-107] ligand-substitution kinetics in K79G report on the heme crevice opening rather than directly on Fe^{III}-S(Met) bond breaking, and this latter step is much faster. Similarly, the observed dynamics during Met80-to-Cys82 ligand substitution in K79G/F82C do not report on Fe^{III}-S(Met) bond breaking, but associated protein rearrangements needed to dissociate Met80 or bind Cys82.

The Three Amino-Acid Ligands X Differ in their Dissociation Kinetics from the Heme Iron. Ligand-substitution reactions of metalloproteins involve dissociation of the ligand from the metal center, binding of the incoming ligand, and conformational rearrangements that support these steps. The positive sign of $\Delta S^{\ddagger}$(X-C) values for all three ligands X in K79G/M80X/F82C reflects the increase in conformational freedom in the transition state. Such a finding is not only expected for the dissociative mechanism of ligand-substitution reactions, but it is also consistent with conformational rearrangements. Since the ligand-substitution reactions studied here take place within the protein scaffold and involve polypeptide dynamics, the $\Delta H^{\ddagger}$(X-C) values are not simply the enthalpies of Fe^{III}-X bond breaking. The large magnitude of these parameters suggests loss of stabilizing interactions (Fe^{III}-X bonds or hydrogen bonds and van der Waals interactions) in all K79G/M80X/F82C variants. Among the three variants the $\Delta H^{\ddagger}$(X-C) value for K79G/M80K*/F82C is the lowest. This result is at odds with the trends we observed in our DFT results (Figure 3A) and may reflect the difference in the nature of the step that govern the kinetics.

Since Lys protonation is typically fast,[115] it is unlikely that this process affects rate constants (and thus activation parameters) observed for the slow Fe^{III}-N(Lys) bond breaking if this step *precedes* Lys protonation. If, however, the bound Lys gets protonated first, the activation parameters will reflect this process. Accounting for the contribution of Lys protonation in K79G/M80K/F82C, we find that the $\Delta H^{\ddagger}$(X-C) values for all three K79G/M80X/F82C variants are similar (Table 5).

In the well-studied alkaline transition of cyt *c*, the back reaction of Lys-ligated to Met-ligated species is rate-limited by Lys dissociation, and the corresponding rate constant k_b reflects the dissociation of Lys ligand in its deprotonated form.[49] Therefore, the activation parameters determined for k_b (Table 5) should truly be Fe^{III}-N(Lys) bond breaking, with no interference from protonation. Interestingly, the $\Delta H^{\ddagger}$ value for the back reaction in the alkaline transition agrees well with those for K79G/F82C and K79G/M80H/F82C variants where protonation step is not a factor (Table 5 and Figure S15). This observation supports our hypothesis that, in K79G/M80K*/F82C, a protonation step is involved and precedes Fe^{III}-N(Lys) bond breaking.

The $\Delta S^{\ddagger}$(X-C) values show large variation among the three variants, but, again, the behavior of K79G/M80K*/F82C is distinct. The much larger $\Delta S^{\ddagger}$(X-C) values for Met and His suggest that polypeptide rearrangement may be relevant for the observed kinetics. Our prior discussion has illustrated that this is the case for K79G/F82C. The greater $\Delta S^{\ddagger}$ values for K79G/M80H/F82C compared to that in unfolded and partially folded cyt *c* (Table 5) suggest that polypeptide rearrangements may play a role for K79G/M80H/F82C as well. Interestingly, while rate constants and $\Delta G^{\ddagger}$ values are similar for our K79G/M80H/F82C variant and other His-ligated proteins, the activation parameters $\Delta H^{\ddagger}$ and $\Delta S^{\ddagger}$ are not, highlighting the importance of temperature-dependence studies in evaluating ligand dissociation kinetics in metalloproteins.

If the rate constant $k^{M\text{-}C}$=34 s^{-1} at room temperature for K79G/F82C reports on heme crevice opening (with a rate constant k_{conf}, Scheme 3) and this process is similar in K79G/M80H/F82C, the rate constant k_{off}^{H} for Fe^{III}-N(His) could be estimated to be about 5.1 s^{-1} (eq 9) for it to yield the apparent rate constant $k^{H\text{-}C}$=4.4 s^{-1}. The comparison (Figure S18A) of Im-bound cyt *c* (PDB ID: 1FI7)[18] and cyt *c* (PDB ID: 1HRC)[116] has revealed a more open heme crevice with the coordination of a bulky Im molecule to the iron center accompanied by loss of a few contacts with heme and contacts between Ω-loops C and D. These structural features agree with differences between K79G/M80H and K79G we observe in our MD simulations of (Figure S18B and S18C) and,

accordingly, we anticipate that the crevice opening in K79G/M80H is faster than that in K79G. Therefore, the rate constant k_{off}^{H}=4.4±0.2 s^{-1} likely reflects Fe^{III}-N(His) bond breaking and its higher value compared to k_{off}^{K}=0.013±0.001 s^{-1} for Fe^{III}-N(Lys) bond breaking is consistent with the relative order of barriers for Fe^{III}-X bond breaking from our DFT calculations (Figure 3A).

Ligands at the Heme Iron Influence Protein Conformational Dynamics. Comparison of wild-type and M100K variants of cyt c_{550} has demonstrated that replacement of the heme iron ligand Met100 with Lys in this protein modifies the structure of the heme coordination loop and results in enhanced flexibility of this region.[117] Our MD models show similar structural differences between ferric Met-ligated K79G and Lys-ligated K79G/M80K* variants of cyt *c* (Figure S6). In K79G/M80K*, contacts between Ω-loops C and D are distinct from those in K79G, implying that the nature of the axial ligand affects interloop connections. Interestingly, the reverse appears to be true as well: conformational properties of Ω-loop C influence the ligand at the heme iron. Multiple studies have now demonstrated effects of mutations in Ω-loop C in cyt *c* on the Met-to-Lys ligand switch in the alkaline transition.[44,105-106,118-120]

Cyt *c* variants with Met, His, and Lys at residue 80 in this work all differ in interresidue connections formed within Ω-loop D and between Ω-loops C and D (Figure S16). Further, the frequencies of these contacts, reflective of protein dynamics, differ depending on the ligand at the heme iron. These results suggest that the identity of the ligand modulates both the structure and dynamics of heme proteins, including those of remote regions, and, thus, ligand-substitution reactions could serve to initiate or switch protein function.

CONCLUSIONS

Ligand dissociation from the metal center is a common regulator of the activity and sensing functions of metalloproteins. Understanding the effects of particular ligands, as well as the polypeptide surrounding, is critical for uncovering mechanisms of these biological processes and exploiting them in the design of biomimetic systems. Our DFT calculations reveal that the ease of breaking metal-ligand interactions in the **6c** heme Fe^{III}-X species increases in the X' series amine < Im < thioether, and that solvent interactions modify the differences in free energy among the **6c** Fe^{III}-X species but do not alter the above sequence. The polypeptide enclosure of the **6c** heme iron species within the cyt *c* scaffold results in a different sequence (Met < Lys < His) for the stability of ferric proteins. Reduction of the heme iron stabilizes the Met-ligated variant but destabilizes the

two other variants, resulting in the Lys < His < Met sequence for ferrous proteins. The distinct direction of the stability change of the protein Met-ligated species upon reduction of the heme iron could be rationalized by the differences in the hydrogen-bonding interactions and in solvation of unbound X in the unfolded proteins.

The substitution of X-to-Cys is gated by conformational rearrangements in K79G/F82C (X=Met) and by processes related to dissociation of X in the two other K79G/M80X/F82C variants (X=His or Lys). The heme crevice opening plays an important role in the overall kinetics of X dissociation, but different Fe^{III}-X bond breaking barriers affect these kinetics as well. As a result, depending on the nature of ligand X, the rate of ligand dissociation in cyt *c* can be tuned by three orders in magnitude. Because heme crevice opening can be accelerated with destabilizing mutations near the heme,[30,105-107] the range of possible rates can be extended even further. These strategies of modulating ligand-substitution rates may be useful in building new molecular switches for catalysis and charge separation.

Thiolate redox-linked switches in this work have allowed for facile determination of kinetics of substitution of endogenous X ligands. In contrast to traditional experiments using small-molecule exogenous ligands to trigger ligand substitutions, equilibrium titrations and multiple kinetic experiments using different concentrations of the ligand are not necessary, accelerating determination of activation parameters. We anticipate that the strategy of using thiolate redox-linked switches for kinetic measurements could facilitate mechanistic efforts with other redox metalloproteins and model complexes.

Acknowledgements. This work was supported by the NSF CHE-1708592 (E.V.P.) grant. S.L.A. thanks the Department of Chemistry and the Office of Undergraduate Research and Advising at Dartmouth College for funding her research. We are grateful to Bruce E. Bowler (University of Montana) for the Rbs (WT*) cyt *c* plasmid.

Supporting Information Available: Seven tables listing free energies of heme models and small-molecule ligands from DFT calculations; heme out-of-plane distortions; EPR *g*-values of cyt *c* variants in this work and related proteins; reduction potentials of cyt *c* variants in this work and related proteins; results of thermal denaturation at pH 5.0; results of thermal denaturation at pH 7.4; comparison of α-helical contents in K79G and K79G/M80X/F82C variants; and eighteen figures showing free energy changes upon binding of amino acids and amino-acid mimics to heme

models and AcMP8; electronic absorption, EPR, and ^{1}H NMR spectra of ferric K79G, M80H, and K79G/M80H; ^{1}H NMR spectra of ferrous M80H, K79G/M80H, and K79G/M80H/F82C at pH 7.4 and 10.0; heat maps of contacts in K79G/M80X; heat maps showing changes in contacts in K79G with M80H and M80K* substitutions and upon reduction of the heme iron; concentration-dependence of observed rate constants k_{obs}^{Az} for Az binding to K79GM80X; pH titrations of ferric K79G/M80X/F82C in the alkaline pH range; CD spectra and melts for K79G/M80X/F82C; MD-derived structural models of K79G/M80X/F82C; solvent exposure of residue 82; heat maps of contacts in ferrous K79G/M80X and K79G/M80X/F82C cyt *c* variants; plots of results from spectroelectrochemistry titrations for K79G/M80X/F82C; relative free energies of ferrous K79G/M80X/F82C; Eyring plots for rate constants $k^{X\text{-}C}$ of K79G/M80K*/F82C at pH 7.4 and 10 and for k_b of *hh* cyt *c*; changes in heme exposure for K79G/M80X during MD simulations; comparison of contacts between Ω-loops C and D in K79G/M80X; hydrogen-bonding networks involving ligand X in ferrous K79G/M80X and K79G/M80X/F82C; changes in contacts upon Im binding to *hh* cyt *c* and with M80H substitution in K79G; and one appendix listing structures and corresponding coordinates of heme models and small-molecule ligands from DFT calculations.

REFERENCES

1. Cherney, M. M.; Bowler, B. E., Protein dynamics and function: Making new strides with an old warhorse, the alkaline conformational transition of cytochrome *c*. *Coord. Chem. Rev.* **2011**, *255*, 664-677.

2. Tang, K.; Knipp, M.; Liu, B.-B.; Cox, N.; Stabel, R.; He, Q.; Zhou, M.; Scheer, H.; Zhao, K.-H.; Gärtner, W., Redox-dependent ligand switching in a sensory heme-binding GAF domain of the cyanobacterium *Nostoc* sp. PCC7120. *J. Biol. Chem.* **2015**, *290*, 19067-19080.

3. Jenner, L. P.; Kurth, J. M.; van Helmont, S.; Sokol, K. P.; Reisner, E.; Dahl, C.; Bradley, J. M.; Butt, J. N.; Cheesman, M. R., Heme ligation and redox chemistry in two bacterial thiosulfate dehydrogenase (TsdA) enzymes. *J. Biol. Chem.* **2019**, *294*, 18002-18014.

4. Kurokawa, H.; Lee, D.-S.; Watanabe, M.; Sagami, I.; Mikami, B.; Raman, C. S.; Shimizu, T., A redox-controlled molecular switch revealed by the crystal structure of a bacterial heme PAS sensor. *J. Biol. Chem.* **2004**, *279*, 20186-20193.

5. Tezcan, F. A.; Winkler, J. R.; Gray, H. B., Effects of ligation and folding on reduction potentials of heme proteins. *J. Am. Chem. Soc.* **1998**, *120*, 13383-13388.

6. Smith, A. T.; Pazicni, S.; Marvin, K. A.; Stevens, D. J.; Paulsen, K. M.; Burstyn, J. N., Functional divergence of heme-thiolate proteins: A classification based on spectroscopic attributes. *Chem. Rev.* **2015**, *115*, 2532-2558.

7. Lisi, G. P.; Hughes, R. P.; Wilcox, D. E., Coordination contributions to protein stability in metal-substituted carbonic anhydrase. *J. Biol. Inorg. Chem.* **2016**, *21*, 659-667.

8. Reddi, A. R.; Gibney, B. R., Role of protons in the thermodynamic contribution of a Zn(II)-Cys_4 site toward metalloprotein stability. *Biochemistry* **2007**, *46*, 3745-3758.

9. Waldner, J. C.; Lahr, S. J.; Edgell, M. H.; Pielak, G. J., Nonideality and protein thermal denaturation. *Biopolymers* **1999**, *49*, 471-479.

10. Gibney, B. R., Chapter eighteen - equilibrium studies of designed metalloproteins. In *Methods Enzymol.*, Pecoraro, V. L., Ed. Academic Press: 2016; Vol. 580, pp 417-438.

11. Battistuzzi, G.; Borsari, M.; Cowan, J. A.; Ranieri, A.; Sola, M., Control of cytochrome *c* redox potential: Axial ligation and protein environment effects. *J. Am. Chem. Soc.* **2002**, *124*, 5315-5324.

12. Feinberg, B. A.; Liu, X.; Ryan, M. D.; Schejter, A.; Zhang, C.; Margoliash, E., Direct voltammetric observation of redox driven changes in axial coordination and intramolecular rearrangement of the phenylalanine-82-histidine variant of yeast iso-1-cytochrome *c*. *Biochemistry* **1998**, *37*, 13091-13101.

13. Creighton, T. E., *Protein structure: a practical approach*. Oxford University Press: 1997.

14. Zhong, F.; Lisi, G. P.; Collins, D. P.; Dawson, J. H.; Pletneva, E. V., Redox-dependent stability, protonation, and reactivity of cysteine-bound heme proteins. *Proc. Natl. Acad. Sci. U. S. A.* **2014**, *111*, E306-315.

15. Sutin, N.; Yandell, J. K., Mechanisms of the reactions of cytochrome *c*: Rate and equilibrium constants for ligand binding to horse heart ferricytochrome *c*. *J. Biol. Chem.* **1972**, *247*, 6932-6936.

16. Kobayashi, K., Pulse radiolysis studies for mechanism in biochemical redox reactions. *Chem. Rev.* **2019**, *119*, 4413-4462.

17. Vos, M. H., Ultrafast dynamics of ligands within heme proteins. *Biochim. Biophys. Acta* **2008**, *1777*, 15-31.

18. Banci, L.; Bertini, I.; Liu, G.; Lu, J.; Reddig, T.; Tang, W.; Wu, Y.; Yao, Y.; Zhu, D., Effects of extrinsic imidazole ligation on the molecular and electronic structure of cytochrome *c*. *J. Biol. Inorg. Chem.* **2001**, *6*, 628-637.

19. Negrerie, M.; Cianetti, S.; Vos, M. H.; Martin, J.-L.; Kruglik, S. G., Ultrafast heme dynamics in ferrous versus ferric cytochrome *c* studied by time-resolved resonance Raman and transient absorption spectroscopy. *J. Phys. Chem. B* **2006**, *110*, 12766-12781.

20. Shimizu, T.; Lengalova, A.; Martínek, V.; Martínková, M., Heme: emergent roles of heme in signal transduction, functional regulation and as catalytic centres. *Chem. Soc. Rev.* **2019**, *48*, 5624-5657.

21. Sun, Y.; Zeng, W.; Benabbas, A.; Ye, X.; Denisov, I.; Sligar, S. G.; Du, J.; Dawson, J. H.; Champion, P. M., Investigations of heme ligation and ligand switching in cytochromes P450 and P420. *Biochemistry* **2013**, *52*, 5941-5951.

22. Zhong, F.; Pletneva, E. V., Ligation and reactivity of methionine-oxidized cytochrome *c*. *Inorg. Chem.* **2018**, *57*, 5754-5766.

23. Yamashita, T.; Hoashi, Y.; Watanabe, K.; Tomisugi, Y.; Ishikawa, Y.; Uno, T., Roles of heme axial ligands in the regulation of CO binding to CcoA. *J. Biol. Chem.* **2004**, *279*, 21394-21400.

24. Kobayashi, K.; Nakagaki, M.; Ishikawa, H.; Iwai, K.; O'Brian, M. R.; Ishimori, K., Redox-dependent dynamics in heme-bound bacterial iron response regulator (Irr) protein. *Biochemistry* **2016**, *55*, 4047-4054.

25. Marvin, K. A.; Kerby, R. L.; Youn, H.; Roberts, G. P.; Burstyn, J. N., The transcription regulator RcoM-2 from *Burkholderia xenovorans* is a cysteine-ligated hemoprotein that undergoes a redox-mediated ligand switch. *Biochemistry* **2008**, *47*, 9016-9028.

26. Zhong, F.; Pletneva, E. V., Mechanistic studies of proton-coupled electron transfer in a calorimetry cell. *J. Am. Chem. Soc.* **2019**, *141*, 9773-9777.

27. Berghuis, A. M.; Brayer, G. D., Oxidation state-dependent conformational changes in cytochrome *c*. *J. Mol. Biol.* **1992**, *223*, 959-976.

28. Zaidi, S.; Hassan, M. I.; Islam, A.; Ahmad, F., The role of key residues in structure, function, and stability of cytochrome-*c*. *Cell. Mol. Life Sci.* **2014**, *71*, 229-255.

29. Louie, G. V.; Pielak, G. J.; Smith, M.; Brayer, G. D., Role of phenylalanine-82 in yeast *iso*-1-cytochrome *c* and remote conformational changes induced by a serine residue at this position. *Biochemistry* **1988**, *27*, 7870-7876.

30. Rafferty, S. P.; Srnith, M.; Mauk, A. G., Azide binding and active site dynamics of position-82 variants of ferricytochrome *c*. *Inorg. Chim. Acta* **1996**, *242*, 171-177.

31. Lalli, D.; Rosa, C.; Allegrozzi, M.; Turano, P., Distal unfolding of ferricytochrome *c* induced by the F82K mutation. *Int. J. Mol. Sci.* **2020**, *21*, 2134.

32. Theorell, H.; Åkesson, Å., Studies on cytochrome *c*. I. Electrophoretic purification of cytochrome *c* and its amino acid composition*. *J. Am. Chem. Soc.* **1941**, *63*, 1804-1811.

33. Theorell, H.; Åkesson, Å., Studies on cytochrome *c*. II. The optical properties of pure cytochrome *c* and some of its derivatives. *J. Am. Chem. Soc.* **1941**, *63*, 1812-1818.

34. Theorell, H.; Åkesson, Å., Studies on cytochrome *c*. III. Titration curves. *J. Am. Chem. Soc.* **1941**, *63*, 1818-1820.

35. Theorell, H., Studies on cytochrome *c*. IV. The magnetic properties of ferric and ferrous cytochrome *c*. *J. Am. Chem. Soc.* **1941**, *63*, 1820-1827.

36. Martinez, R. E.; Bowler, B. E., Proton-mediated dynamics of the alkaline conformational transition of yeast *iso*-1-cytochrome *c*. *J. Am. Chem. Soc.* **2004**, *126*, 6751-6758.

37. Rosell, F. I.; Ferrer, J. C.; Mauk, A. G., Proton-linked protein conformational switching: Definition of the alkaline conformational transition of yeast *iso*-1-ferricytochrome *c*. *J. Am. Chem. Soc.* **1998**, *120*, 11234-11245.

38. Van Rossum, G. a. D., Fred L., *Python 3 reference manual*. CreateSpace: Scotts Valley, CA, 2009.

39. Pettersen, E. F.; Goddard, T. D.; Huang, C. C.; Couch, G. S.; Greenblatt, D. M.; Meng, E. C.; Ferrin, T. E., UCSF Chimera—A visualization system for exploratory research and analysis. *J. Comput. Chem.* **2004**, *25*, 1605-1612.

40. Duncan, M. G.; Williams, M. D.; Bowler, B. E., Compressing the free energy range of substructure stabilities in *iso*-1-cytochrome *c*. *Protein Sci.* **2009**, *18*, 1155-1164.

41. Amacher, J. F.; Zhong, F.; Lisi, G. P.; Zhu, M. Q.; Alden, S. L.; Hoke, K. R.; Madden, D. R.; Pletneva, E. V., A compact structure of cytochrome *c* trapped in a lysine-ligated state: Loop

refolding and functional implications of a conformational switch. *J. Am. Chem. Soc.* **2015**, *137*, 8435-8449.

42. Hanske, J.; Toffey, J. R.; Morenz, A. M.; Bonilla, A. J.; Schiavoni, K. H.; Pletneva, E. V., Conformational properties of cardiolipin-bound cytochrome *c*. *Proc. Natl. Acad. Sci. USA* **2012**, *109*, 125-130. .

43. Berry, E. A.; Trumpower, B. L., Simultaneous determination of hemes *a*, *b*, and *c* from pyridine hemochrome spectra. *Anal. Biochem.* **1987**, *161*, 1-15.

44. Gu, J.; Shin, D. W.; Pletneva, E. V., Remote perturbations in tertiary contacts trigger ligation of lysine to the heme iron in cytochrome *c*. *Biochemistry* **2017**, *56*, 2950-2966.

45. Wendt, H.; Leder, L.; Härmä, H.; Jelesarov, I.; Baici, A.; Bosshard, H. R., Very rapid, ionic strength-dependent association and folding of a heterodimeric leucine zipper. *Biochemistry* **1997**, *36*, 204-213.

46. Solomon, L. A.; Kodali, G.; Moser, C. C.; Dutton, P. L., Engineering the assembly of heme cofactors in man-made proteins. *J. Am. Chem. Soc.* **2014**, *136*, 3192-3199.

47. Welch, T. W.; Thorp, H. H., Distribution of metal complexes bound to DNA determined by normal pulse voltammetry. *J. Phys. Chem.* **1996**, *100*, 13829-13836.

48. Appleby, C. A.; Morton, R. K., Lactic dehydrogenase and cytochrome b_2 of baker's yeast. Purification and crystallization. *Biochem. J* **1959**, *71*, 492-499.

49. Davis, L. A.; Schejter, A.; Hess, G. P., Alkaline isomerization of oxidized cytochrome *c*: Equilibrium and kinetic measurements. *J. Biol. Chem.* **1974**, *249*, 2624-2632.

50. Louie, G. V.; Brayer, G. D., High-resolution refinement of yeast *iso*-1-cytochrome *c* and comparisons with other eukaryotic cytochromes *c*. *J. Mol. Biol.* **1990**, *214*, 527-555.

51. Mackerell Jr, A. D.; Feig, M.; Brooks Iii, C. L., Extending the treatment of backbone energetics in protein force fields: Limitations of gas-phase quantum mechanics in reproducing protein conformational distributions in molecular dynamics simulations. *J. Comput. Chem.* **2004**, *25*, 1400-1415.

52. Autenrieth, F.; Tajkhorshid, E.; Baudry, J.; Luthey-Schulten, Z., Classical force field parameters for the heme prosthetic group of cytochrome *c*. *J. Comput. Chem.* **2004**, *25*, 1613-1622.

53. Deng, Y. Effects of heme propionates on structural and redox properties of *c*-type cytochromes. Dartmouth College, 2020.

54. MacKerell, A. D.; Bashford, D.; Bellott, M.; Dunbrack, R. L.; Evanseck, J. D.; Field, M. J.; Fischer, S.; Gao, J.; Guo, H.; Ha, S.; Joseph-McCarthy, D.; Kuchnir, L.; Kuczera, K.; Lau, F. T. K.; Mattos, C.; Michnick, S.; Ngo, T.; Nguyen, D. T.; Prodhom, B.; Reiher, W. E.; Roux, B.; Schlenkrich, M.; Smith, J. C.; Stote, R.; Straub, J.; Watanabe, M.; Wiórkiewicz-Kuczera, J.; Yin,

D.; Karplus, M., All-atom empirical potential for molecular modeling and dynamics studies of proteins. *J. Phys. Chem. B* **1998**, *102*, 3586-3616.

55. Michaud-Agrawal, N.; Denning, E. J.; Woolf, T. B.; Beckstein, O., MDAnalysis: A toolkit for the analysis of molecular dynamics simulations. *J. Comput. Chem.* **2011**, *32*, 2319-2327.

56. Andersson, M. P.; Uvdal, P., New scale factors for harmonic vibrational frequencies using the B3LYP density functional method with the triple-ζ basis set 6-311+G(d,p). *J. Phys. Chem. A* **2005**, *109*, 2937-2941.

57. Stephens, P. J.; Devlin, F. J.; Chabalowski, C. F.; Frisch, M. J., *Ab initio* calculation of vibrational absorption and circular dichroism spectra using density functional force fields. *J. Phys. Chem.* **1994**, *98*, 11623-11627.

58. Becke, A. D., A new mixing of Hartree-Fock and local-density-functional theories. *J. Chem. Phys.* **1993**, *98*, 1372-1377.

59. Becke, A. D., Density-functional thermochemistry. III. The role of exact exchange. *J. Chem. Phys.* **1993**, *98*, 5648-5652.

60. Lee, C.; Yang, W.; Parr, R. G., Development of the Colle-Salvetti correlation-energy formula into a functional of the electron density. *Phys. Rev. B* **1988**, *37*, 785-789.

61. Goerigk, L.; Grimme, S., A thorough benchmark of density functional methods for general main group thermochemistry, kinetics, and noncovalent interactions. *Phys. Chem. Chem. Phys.* **2011**, *13*, 6670-6688.

62. Grimme, S.; Antony, J.; Ehrlich, S.; Krieg, H., A consistent and accurate ab initio parametrization of density functional dispersion correction (DFT-D) for the 94 elements H-Pu. *J. Chem. Phys* **2010**, *132*, 154104.

63. Wadt, W. R.; Hay, P. J., Ab initio effective core potentials for molecular calculations. Potentials for main group elements sodium to bismuth. *J. Chem. Phys.* **1985**, *82*, 284-298.

64. Hay, P. J.; Wadt, W. R., Ab initio effective core potentials for molecular calculations. Potentials for potassium to gold including the outermost core orbitals. *J. Chem. Phys.* **1985**, *82*, 299-310.

65. Hay, P. J.; Wadt, W. R., Ab initio effective core potentials for molecular calculations. Potentials for the transition metal atoms scandium to mercury. *J. Chem. Phys.* **1985**, *82*, 270-283.

66. Dunning, T. H.; Hay, P. J., *Modern Theoretical Chemistry, Vol. 4: Applications of Electronic Structure Theory*. Plenum, NY: 1977; p 461.

67. Frisch, M. J.; Pople, J. A.; Binkley, J. S., Self-consistent molecular orbital methods. 25. Supplementary functions for Gaussian basis sets. *J. Chem. Phys.* **1984**, *80*, 3265-3269.

68. Clark, T.; Chandrasekhar, J.; Spitznagel, G. W.; Schleyer, P. v. R., Efficient diffuse function-augmented basis sets for anion calculations. III. The 3-21 + G basis set for first-row elements, lithium to fluorine. *J. Comput. Chem.* **1983**, *4*, 294-301.

69. McLean, A. D.; Chandler, G. S., Contracted Gaussian basis sets for molecular calculations. I. Second row atoms, Z = 11-18. *J, Chem. Phys.* **1980**, *72*, 5639-5648.

70. Krishnan, R.; Binkley, J. S.; Seeger, R.; Pople, J. A., Self-consistent molecular orbital methods. XX. A basis set for correlated wave functions. *J. Chem. Phys.* **1980**, *72*, 650-654.

71. Bochevarov, A. D.; Harder, E.; Hughes, T. F.; Greenwood, J. R.; Braden, D. A.; Philipp, D. M.; Rinaldo, D.; Halls, M. D.; Zhang, J.; Friesner, R. A., Jaguar: A high-performance quantum chemistry software program with strengths in life and materials sciences. *Int. J. Quantum Chem* **2013**, *113*, 2110-2142.

72. *Jaguar, versions 7.0-9.6*, Schrödinger, LLC, New York, NY: 2007-2018.

73. Ali, M. E.; Sanyal, B.; Oppeneer, P. M., Electronic structure, spin-states, and spin-crossover reaction of heme-related Fe-Porphyrins: A theoretical perspective. *J. Phys. Chem. B* **2012**, *116*, 5849-5859.

74. Zoppellaro, G.; Bren, K. L.; Ensign, A. A.; Harbitz, E.; Kaur, R.; Hersleth, H.-P.; Ryde, U.; Hederstedt, L.; Andersson, K. K., Review: Studies of ferric heme proteins with highly anisotropic/highly axial low spin (S = 1/2) electron paramagnetic resonance signals with bis-Histidine and histidine-methionine axial iron coordination. *Biopolymers* **2009**, *91*, 1064-1082.

75. Tannor, D. J.; Marten, B.; Murphy, R.; Friesner, R. A.; Sitkoff, D.; Nicholls, A.; Honig, B.; Ringnalda, M.; Goddard, W. A., Accurate first principles calculation of molecular charge distributions and solvation energies from Ab initio quantum mechanics and continuum dielectric theory. *J. Am. Chem. Soc.* **1994**, *116*, 11875-11882.

76. Marten, B.; Kim, K.; Cortis, C.; Friesner, R. A.; Murphy, R. B.; Ringnalda, M. N.; Sitkoff, D.; Honig, B., A new model for calculation of solvation free energies: Correction of self-consistent reaction field continuum dielectric theory for short range hydrogen-bonding effects. *J. Phys. Chem.* **1996**, *100*, 11775-11788.

77. Christensen, J. J.; Izatt, R. M.; Wrathall, D. P.; Hansen, L. D., Thermodynamics of proton ionization in dilute aqueous solution. Part XI. pK, $\Delta H°$, and $\Delta S°$ values for proton ionization from protonated amines at 25°. *J. Chem Soc. A* **1969**, 1212-1223.

78. Shankar, R.; Senthilkumar, K.; Kolandaivel, P., Calculation of ionization potential and chemical hardness: A comparative study of different methods. *Int. J. Quantum Chem* **2009**, *109*, 764-771.

79. Kruglik, S. G.; Yoo, B.-K.; Lambry, J.-C.; Martin, J.-L.; Negrerie, M., Structural changes and picosecond to second dynamics of cytochrome *c* in interaction with nitric oxide in ferrous and ferric redox states. *PCCP* **2017**, *19*, 21317-21334.

80. Jentzen, W.; Ma, J.-G.; Shelnutt, J. A., Conservation of the conformation of the porphyrin macrocycle in hemoproteins. *Biophys. J.* **1998**, *74*, 753-763.

81. Liptak, M. D.; Wen, X.; Bren, K. L., NMR and DFT investigation of heme ruffling: Functional implications for cytochrome *c*. *J. Am. Chem. Soc.* **2010**, *132*, 9753-9763.

82. Kleingardner, J. G.; Levin, B. D.; Zoppellaro, G.; Andersson, K. K.; Elliott, S. J.; Bren, K. L., Influence of heme *c* attachment on heme conformation and potential. *J. Biol. Inorg. Chem.* **2018**, *23*, 1073-1083.

83. Bowman, S. E. J.; Bren, K. L., The chemistry and biochemistry of heme *c*: functional bases for covalent attachment. *Nat. Prod. Rep.* **2008**, *25*, 1118-1130.

84. Kleingardner, J. G.; Bren, K. L., Biological significance and applications of heme *c* proteins and peptides. *Acc. Chem. Res.* **2015**, *48*, 1845-1852.

85. Silkstone, G. G.; Cooper, C. E.; Svistunenko, D.; Wilson, M. T., EPR and optical spectroscopic studies of Met80X mutants of yeast ferricytochrome *c*. Models for intermediates in the alkaline transition. *J. Am. Chem. Soc.* **2005**, *127*, 92-99.

86. Hawkins, B. K.; Hilgen-Willis, S.; Pielak, G. J.; Dawson, J. H., Novel axial ligand interchange in cytochrome *c*: incorporation of a histidine at position 82 leads to displacement of the wild-type methionine-80 ligand. *J. Am. Chem. Soc.* **1994**, *116*, 3111-3112.

87. Kumar, R.; Matsumura, H.; Lovell, S.; Yao, H.; Rodríguez, J. C.; Battaile, K. P.; Moënne-Loccoz, P.; Rivera, M., Replacing the axial ligand Tyrosine 75 or its hydrogen bond partner Histidine 83 minimally affects hemin acquisition by the hemophore HasAp from *Pseudomonas aeruginosa*. *Biochemistry* **2014**, *53*, 2112-2125.

88. Deng, Y.; Zhong, F.; Alden, S. L.; Hoke, K. R.; Pletneva, E. V., The K79G mutation reshapes the heme crevice and alters redox properties of cytochrome *c*. *Biochemistry* **2018**, *57*, 5827-5840.

89. McClelland, L. J.; Mou, T.-C.; Jeakins-Cooley, M. E.; Sprang, S. R.; Bowler, B. E., Structure of a mitochondrial cytochrome *c* conformer competent for peroxidase activity. *Proc. Natl. Acad. Sci. USA* **2014**, *111*, 6648.

90. Marques, H. M.; Cukrowski, I.; Vashi, P. R., Co-ordination of weak field ligands by N-acetylmicroperoxidase-8 (NAcMP8), a ferric haempeptide from cytochrome *c*, and the influence of the axial ligand on the reduction potential of complexes of NAcMP8. *J. Chem. Soc., Dalton Trans.* **2000**, 1335-1342.

91. Nakajima, H.; Honma, Y.; Tawara, T.; Kato, T.; Park, S.-Y.; Miyatake, H.; Shiro, Y.; Aono, S., Redox properties and coordination structure of the heme in the CO-sensing transcriptional activator CooA*. *J. Biol. Chem.* **2001**, *276*, 7055-7061.

92. Koppenhöfer, A.; Turner, K. L.; Allen, J. W. A.; Chapman, S. K.; Ferguson, S. J., Cytochrome cd_1 from *Paracoccus pantotrophus* exhibits kinetically gated, conformationally dependent, highly cooperative two-electron redox behavior. *Biochemistry* **2000**, *39*, 4243-4249.

93. Machado, T. F. G.; Gloster, T. M.; da Silva, R. G., Linear Eyring plots conceal a change in the rate-limiting step in an enzyme reaction. *Biochemistry* **2018**, *57*, 6757-6761.

94. Satterlee, J. D.; La Mar, G. N.; Bold, T. J., Dynamics and thermodynamics of axial ligation in metalloporphyrins. 6. Axial lability of nitrogenous bases in low-spin ferric complexes and the role of five-coordinate transient species. *J. Am. Chem. Soc.* **1977**, *99*, 1088-1093.

95. Abbruzzetti, S.; Viappiani, C.; Small, J. R.; Libertini, L. J.; Small, E. W., Kinetics of histidine deligation from the heme in GuHCl-unfolded Fe(III) cytochrome *c* studied by a laser-induced pH-jump technique. *J. Am. Chem. Soc.* **2001**, *123*, 6649-6653.

96. Colón, W.; Wakem, L. P.; Sherman, F.; Roder, H., Identification of the predominant non-native histidine ligand in unfolded cytochrome *c*. *Biochemistry* **1997**, *36*, 12535-12541.

97. Dumortier, C.; Meyer, T. E.; Cusanovich, M. A., Protein dynamics: imidazole binding to class I *c*-type cytochromes. *Arch. Biochem. Biophys.* **1999**, *371*, 142-148.

98. Kroll, T.; Hadt, R. G.; Wilson, S. A.; Lundberg, M.; Yan, J. J.; Weng, T.-C.; Sokaras, D.; Alonso-Mori, R.; Casa, D.; Upton, M. H.; Hedman, B.; Hodgson, K. O.; Solomon, E. I., Resonant inelastic x-ray scattering on ferrous and ferric bis-imidazole porphyrin and cytochrome *c*: Nature and role of the axial methionine–fe bond. *J. Am. Chem. Soc.* **2014**, *136*, 18087-18099.

99. Tozer, D. J.; De Proft, F., Computation of the hardness and the problem of negative electron affinities in density functional theory. *J. Phys. Chem. A* **2005**, *109*, 8923-8929.

100. Baidya, M.; Brotzel, F.; Mayr, H., Nucleophilicities and Lewis basicities of imidazoles, benzimidazoles, and benzotriazoles. *Org. Biomol. Chem.* **2010**, *8*, 1929-1935.

101. Marques, H. M., Insights into porphyrin chemistry provided by the microperoxidases, the haempeptides derived from cytochrome *c*. *Dalton Trans.* **2007**, 4371-4385.

102. Mara, M. W.; Hadt, R. G.; Reinhard, M. E.; Kroll, T.; Lim, H.; Hartsock, R. W.; Alonso-Mori, R.; Chollet, M.; Glownia, J. M.; Nelson, S.; Sokaras, D.; Kunnus, K.; Hodgson, K. O.; Hedman, B.; Bergmann, U.; Gaffney, K. J.; Solomon, E. I., Metalloprotein entatic control of ligand-metal bonds quantified by ultrafast X-ray spectroscopy. *Science* **2017**, *356*, 1276-1280.

103. Wolfenden, R.; Andersson, L.; Cullis, P. M.; Southgate, C. C. B., Affinities of amino acid side chains for solvent water. *Biochemistry* **1981**, *20*, 849-855.

104. Viola, F.; Aime, S.; Coletta, M.; Desideri, A.; Fasano, M.; Paoletti, S.; Tarricone, C.; Ascenzi, P., Azide, cyanide, fluoride, imidazole and pyridine binding to ferric and ferrous native horse heart cytochrome *c* and to its carboxymethylated derivative: A comparative study. *J. Inorg. Biochem.* **1996**, *62*, 213-222.

105. Deacon, O. M.; Svistunenko, D. A.; Moore, G. R.; Wilson, M. T.; Worrall, J. A. R., Naturally occurring disease-related mutations in the 40–57 Ω-loop of human cytochrome *c* control triggering of the alkaline isomerization. *Biochemistry* **2018**, *57*, 4276-4288.

106. Deacon, O. M.; Karsisiotis, A. I.; Moreno-Chicano, T.; Hough, M. A.; Macdonald, C.; Blumenschein, T. M. A.; Wilson, M. T.; Moore, G. R.; Worrall, J. A. R., Heightened dynamics of the oxidized Y48H variant of human cytochrome *c* increases its peroxidatic activity. *Biochemistry* **2017**, *56*, 6111-6124.

107. Karsisiotis, A. I.; Deacon, O. M.; Wilson, M. T.; Macdonald, C.; Blumenschein, T. M. A.; Moore, G. R.; Worrall, J. A. R., Increased dynamics in the 40–57 Ω-loop of the G41S variant of human cytochrome *c* promote its pro-apoptotic conformation. *Sci. Rep.* **2016**, *6*, 30447.

108. Pearce, L. L.; Gartner, A. L.; Smith, M.; Mauk, A. G., Mutation-induced perturbation of the cytochrome *c* alkaline transition. *Biochemistry* **1989**, *28*, 3152-3156.

109. Dumortier, C.; Fitch, J.; Petegem, F. V.; Vermeulen, W.; Meyer, T. E.; Van Beeumen, J. J.; Cusanovich, M. A., Protein dynamics in the region of the sixth ligand methionine revealed by studies of imidazole binding to *Rhodobacter capsulatus* cytochrome c_2 hinge mutants. *Biochemistry* **2004**, *43*, 7717-7724.

110. Dumortier, C.; Holt, J. M.; Meyer, T. E.; Cusanovich, M. A., Imidazole binding to *Rhodobacter capsulatus* cytochrome c_2: Effect of site-directed mutants on ligand binding. *J. Biol. Chem.* **1998**, *273*, 25647-25653.

111. Cherney, M. M.; Junior, C. C.; Bergquist, B. B.; Bowler, B. E., Dynamics of the His79-heme alkaline transition of yeast *iso*-1-cytochrome *c* probed by conformationally gated electron transfer with Co(II)bis(terpyridine). *J. Am. Chem. Soc.* **2013**, *135*, 12772-12782.

112. Bandi, S.; Bowler, B. E., A cytochrome *c* electron transfer switch modulated by heme ligation and isomerization of a peptidyl-prolyl bond. *Peptide Science* **2013**, *100*, 114-124.

113. Bandi, S.; Bowler, B. E., Probing the dynamics of a His73–heme alkaline transition in a destabilized variant of yeast *iso*-1-cytochrome *c* with conformationally gated electron transfer methods. *Biochemistry* **2011**, *50*, 10027-10040.

114. Leavens, M. J.; Cherney, M. M.; Finnegan, M. L.; Bowler, B. E., Probing denatured state conformational bias in a three-helix bundle, UBA(2), using a cytochrome *c* fusion protein. *Biochemistry* **2018**, *57*, 1711-1721.

115. Borisenko, V.; Sansom, M. S. P.; Andrew Woolley, G., Protonation of lysine residues inverts cation/anion selectivity in a model channel. *Biophys. J.* **2000**, *78*, 1335-1348.

116. Bushnell, G. W.; Louie, G. V.; Brayer, G. D., High-resolution three-dimensional structure of horse heart cytochrome *c*. *J. Mol. Biol.* **1990**, *214*, 585-595.

117. Worrall, J. A. R.; van Roon, A.-M. M.; Ubbink, M.; Canters, G. W., The effect of replacing the axial methionine ligand with a lysine residue in cytochrome *c*-550 from *Paracoccus versutus* assessed by X-ray crystallography and unfolding. *FEBS J.* **2005**, *272*, 2441-2455.

118. Lou, D.; Liu, X.-C.; Wang, X.-J.; Gao, S.-Q.; Wen, G.-B.; Lin, Y.-W., The importance of Asn52 in the structure–function relationship of human cytochrome *c*. *RSC Advances* **2020**, *10*, 44768-44772.

119. Lei, H.; Bowler, B. E., Naturally occurring A51V variant of human cytochrome *c* destabilizes the native state and enhances peroxidase activity. *J. Phys. Chem. B* **2019**, *123*, 8939-8953.

120. Deng, Y.; Weaver, M. L.; Hoke, K. R.; Pletneva, E. V., A heme propionate staples the structure of cytochrome *c* for methionine ligation to the heme iron. *Inorg. Chem.* **2019**, *58*, 14085-14106.

Table of Content Graphics

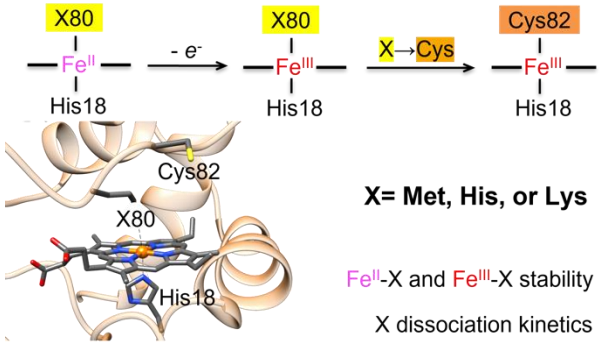

SYNOPSYS

Thiolate redox-linked switches were engineered in cytochrome *c* to compare properties of Met-, His-, and Lys-ligated ferric hemes and elucidate the role of heme crevice dynamics in ligand-substitution reactions. Analyses of thermal denaturation and reduction potentials of switchable and non-switchable variants ranked stabilities of differently-ligated ferric and ferrous species. Small-molecule ligand substitution experiments and theoretical studies were used to validate the use of thiolate switches for kinetic studies and to rationalize the observed trends.